Gondwana Research 129 (2024) 142–166

Contents lists available at ScienceDirect

Gondwana Research

journal homepage: www.elsevier.com/locate/gr

Chemo- and bio-stratigraphic constraints on Cretaceous-Paleocene biotic turnover in the southern Tethys low-oxygen margin, Egypt

Moataz El-Shafeiy [a,b,*], Daizhao Chen [a,c], Zhuyin Chu [d], Mu Liu [a], Ramadan M. El-Kahawy [b]

[a] Key Laboratory of Cenozoic Geology and Environment, Institute of Geology and Geophysics, Chinese Academy of Sciences, Beijing 100029, China
[b] Geology Department, Faculty of Sciences, Cairo University, Giza 12613, Egypt
[c] University of Chinese Academy of Sciences, Beijing 100049, China
[d] Key Laboratory of Lithospheric Evolution, Institute of Geology and Geophysics, Chinese Academy of Sciences, Beijing 100029, China

ARTICLE INFO

Article history:
Received 8 June 2023
Revised 27 November 2023
Accepted 18 December 2023
Available online 22 December 2023
Handling editor: Damian Nance

Keywords:
K-Pg transition
Organic-rich sequence
Chemo-biostratigraphy
Mo-U covariation
C-N-S isotopes
Re/Os system

ABSTRACT

The late Cretaceous-Danian (K-Pg) organic-rich sequence is a global archive that witnessed abrupt paleo-condition changes during a high sea-level. In Egypt, this sequence is present in the Duwi and Dakhla formations as an E-W belt from the Red Sea to the Western Desert. We analyzed elemental and isotopic distributions in an age-constrained core from the Quseir area to understand paleoclimatic and paleoenvironmental factors influencing its deposition. Calcareous nannofossil and the chemical index of alteration (CIA) confirm a global cooling trend during the late Cretaceous, with two warming episodes indicating early phases of the Deccan volcanism. The Danian stage experienced a warm climate and intense chemical weathering. Mo-U enrichment factors covariation suggest deposition under oxygen-deficient conditions with evident watermass restrictions. High-productivity-indicating taxa were more abundant in Danian strata than in late Cretaceous strata, consistent with organic carbon characteristics. The $\delta^{13}C_{Org}$-$\delta^{15}N$ data show temporal heterogeneity due to organic matter type, redox conditions, preservation, stratigraphic condensation, and recycling of isotopically-light CO_2. The negative $\delta^{13}C_{Org}$ shift around the K-Pg transition is globally correlative. Dynamic pyrite $\delta^{34}S$ distribution resulted from variation in riverine influx, degree of pore-water openness, sulfate reduction rate, and diagenetic disproportionation of sulfur intermediates. Generally, radiogenic $^{187}Os/^{188}Os$ values were observed that were seemingly influenced by continental weathering and subsequent runoff influx of $^{187}Os/^{188}Os$ under a greenhouse climate. A positive $^{187}Os/^{188}Os$ shift to 3.68 ($^{187}Os/^{188}Os_i$ of 0.74) occurred at the onset of the Dakhla organic-rich spike. However, without a precise correlative stratigraphic framework, a global or regional seawater isotopic shift cannot be confirmed. We suggest that temporal variations in organic matter composition, redox, watermass conditions, and isotope fractionation of the K-Pg sequence in the study area were driven by discrepancies in climate, sea-level, and tectonic uplift. Further integrated approaches are needed to explore the geospheric drivers of this organic-rich sequence in time-equivalent sections.

1. Introduction

The late Cretaceous-early Paleocene (K-Pg) period was characterized by a greenhouse climate, marked by elevated CO_2 levels resulting from the Deccan extensive volcanism. Notably, this volcanism exhibited two major phases during the late Cretaceous and one major phase during the early Paleocene (Takashima et al., 2006; Keller et al., 2011). This period witnessed a rapid decline in marine phytoplanktonic assemblages that coincided with a global mass extinction event associated with the Deccan intense volcanism and the Chicxulub impact, which severely impacted the biodiversity (Keller, 2003; Falkowski et al., 2004). Recent refinements in dating the Deccan trap eruptions indicate that the most intensive phase occurred more than 100 ka prior to the K-Pg transition, suggesting that CO_2 contributions from the Deccan volcanism may have been underestimated (Ravizza and Peucker-Ehrenbrink, 2003). In addition to volcanic activity, the K-Pg period witnessed significant climatic and geochemical changes, representing a pivotal period in Earth's history. These changes encompassed various phenomena, including stable isotope perturbations (Keller et al., 2002; Meilijson et al., 2018), fluctuations in

* Corresponding author at: Key Laboratory of Cenozoic Geology and Environment, Institute of Geology and Geophysics, Chinese Academy of Sciences, Beijing 100029, China.
E-mail address: motazadel80@cu.edu.eg (M. El-Shafeiy).

https://doi.org/10.1016/j.gr.2023.12.007
1342-937X/

climate and sea-levels (Adatte et al., 2002), turnover in faunal and phytoplanktonic communities (Keller et al., 1998; Keller et al., 2002; Tantawy, 2003; Sepúlveda, 2008; Sepúlveda et al., 2009; El-Shafeiy et al., 2014; Abu-Ali et al., 2019), and the development of regional marine anoxia leading to the accumulation of organic-rich sequences (El-Shafeiy et al., 2016; 2017; Fathy et al., 2023a).

The process of sedimentary organic-rich accumulation is influenced by various factors including bioproductivity, paleo-redox conditions, water column stratification, oceanic currents, and sedimentation rate (Sepúlveda et al., 2009; Littke and Zieger, 2020). During accumulation, the removal of redox-sensitive elements from the water, such as Mo, U, Re, and Os, through both biotic and abiotic pathways resulted in their sequestration within the sediment (Tribovillard et al., 2006). The sediment records of these processes are commonly employed as indicators of paleo-redox conditions in marine environments and are referred to as paleoceanographic proxies (Brumsack, 2006; Algeo and Rowe, 2012). Furthermore, organic-rich sediments have Re and Os concentrations that are significantly higher, by ≥ 2 orders of magnitude, than those found in the average continental crust (Sun et al., 2003; Baioumy et al., 2011). Additionally, $^{187}Re/^{188}Os$ ratios are typically 1–2 orders of magnitude greater than those of average continental crust materials (Peucker-Ehrenbrink and Ravizza, 2002). These elements have a primarily hydrogenous origin and can become associated with organic matter in sediment through their sequestration (Yamashita et al., 2007). The variable redox-driven speciation of Re and Os makes them potentially useful as indicators of seawater Re-Os paleo-system proxies (Selby and Creaser, 2003).

Chemostratigraphic investigations of stable isotope geochemistry offer valuable insights into correlating regional and global sections, as well as into the exploration of paleoenvironmental variations (e.g., Keller et al., 2016). The release of high concentrations of CO_2 (3–4 times present-day level) accompanied by low $\delta^{13}C$ values is attributed to the Deccan volcanism, which caused warming during the K-Pg period (Nordt et al., 2003). However, certain studies have found no compelling evidence supporting a significant pulse of atmospheric CO_2 coinciding with the K-Pg event (Milligan et al., 2019). Nevertheless, certain records do support a negative $\delta^{13}C$ excursion, coupled with a warming period and a decline in osmium isotope values around the K-Pg transition (Robinson et al., 2009; Henehan et al., 2016; Barnet et al., 2018; Hull et al., 2020). In addition to carbon, fixed nitrogen incorporation is crucial for photosynthesis in various organisms. The nitrate anion plays a vital role as an oxidant in the biogeochemical cycle within the oxygen minimum zone of modern oceans (Canfield et al., 2010), making it valuable to understand the nitrogen isotope composition in sedimentary organic matter (Pinti and Hashizume, 2011; Robinson et al., 2012). Changes in nitrogen isotopes provide insights into variations in marine nitrogen geochemistry, including denitrification, nitrogen fixation, and nutrient consumption (Meilijson et al., 2018; Sepúlveda et al., 2019). Therefore, further research employing $\delta^{15}N$ is needed to establish a comprehensive isotopic trend and unravel changes in the marine nitrogen cycle during the K-Pg oxygen-deficient sedimentary record.

During the K-Pg time, a marine epicontinental shelf dominated the central part of Egypt (Fig. 1). Sedimentation in this area was influenced by global warming and high sea-level, which resulted in the development of anoxic conditions within the marine system (Robinson and Engel, 1993; Issawi and Farouk, 2023). Consequently, organic matter-rich layers and phosphorite were deposited, primarily confined to the Duwi Formation and the overlying Dakhla Formation in Central Egypt, as a part of North Africa and the Middle East region, constituted a unique K-Pg sequence of sediment (Robinson and Engel, 1993; Issawi and Farouk, 2023). This study focuses on examining the elemental and isotopic secular variations within the Duwi and Dakhla formations along the Qseir K-Pg organic-rich sequence. The investigation utilizes a shallow core drilled in the Duwi mountain area (Fig. 2) to undertake a comprehensive analysis of isotope perturbations, as well as paleo-redox conditions, to reveal crucial stages in the accumulation of the organic-rich sequence during the K-Pg period. For the first time, we employ a combination of elemental proxies, bulk $\delta^{13}C_{Org}$, $\delta^{15}N$ data, pyrite $\delta^{34}S$ data, Re/Os system, and calcareous nannofossil biozonation to decipher fluctuations in marine paleoproductivity, paleoclimate, and paleo-redox conditions that record the major paleoenvironmental changes prevailed during this period.

2. Geologic setting

The K-Pg organic-rich succession in Egypt forms an east–west belt that stretches from the Red Sea coast in the Qseir-Safaga area to the Kharga-Dakhla landstretch (Figs. 1-2A). These sediments are primarily found within the Duwi Formation and the overlying Dakhla Formation. The Duwi Formation is part of a phosphogenic belt that extends across the Middle East to North Africa (Baioumy and Tada, 2005). It comprises organic-rich shale, glauconite and/or oyster limestone, chert, siltstone, and phosphatic layers (Abed and Al-Agha, 1989; Glenn and Arthur, 1990; El-Kammar, 1993; El-Shafeiy et al., 2014; 2016, among others). This lithology is indicative of a zone of high marine primary production due to an upwelling system along paleo-highs that brought deep, cool, nutrient-rich waters to the surface water layer during this period (e.g., Ganz, 1984; Germann et al., 1985; Abed, 2013; Fathy et al., 2023a). Other studies have proposed that fluvially-induced nutrients, supplied from a highly weathered continent, were the main driver that promoted photic zone productivity during that period (e.g., Glenn and Arthur, 1990). Wind-induced upwelling and runoff may both have contributed as nutrient supplies to the southern Tethys margins during the late Cretaceous (Robinson, 1995).

The Duwi Formation is classified into four members by Baioumy and Tada (2005) based on distinct sedimentary characteristics. The Lower Member represents the initial transgressive cycle, and the Middle Member exhibits organic-rich shale indicative of a high-stand systems tract (HST) stage. The transition from the Middle to Upper members marks the beginning of a regressive phase, corresponding to a lowstand systems tract (LST). The second transgressive cycle is observed at the base of the Uppermost Member, which extends into the conformably overlying Dakhla Formation (El-Shafeiy et al., 2014). The Dakhla Formation comprises the Hamama and Beida members in ascending order, separated by an unconformity marking the K-Pg transition (Abdel Razik, 1972; Luger, 1988; Awad et al., 1992; Zalat et al., 2008). In terms of lithology, the Dakhla Formation is primarily characterized by deeper epicontinental shale and/or marl with intermittent occurrences of limestone and subordinate siltstone (El-Shafeiy, 2012). Zalat et al. (2008) identified two cycles of increasing depth within the Dakhla Formation, corresponding to the Hamama and Beida members. The biostratigraphic analysis of dinoflagellates, nanoplankton, foraminiferal assemblages, and palynoforms indicates that the Duwi Formation spans the Campanian to early Maastrichtian, while the Dakhla Formation covers the Maastrichtian to early Paleocene (e.g., El-Shafeiy et al., 2014; 2017; Abu Ali et al., 2019). Moreover, dinoflagellate cysts (dinocysts) in the studied Qseir core indicate marine origin and very high paleo-productivity time (Tahoun and Mohamed, 2020). Regarding organic material investigations (El-Shafeiy, 2012; El-Shafeiy et al., 2014; 2017), the Qseir section analyzed encompasses kerogen type III (Upper Member of Duwi Formation), type II (majority of Dakhla Formation with Lower and Middle members of Duwi Formation), and type I (por-

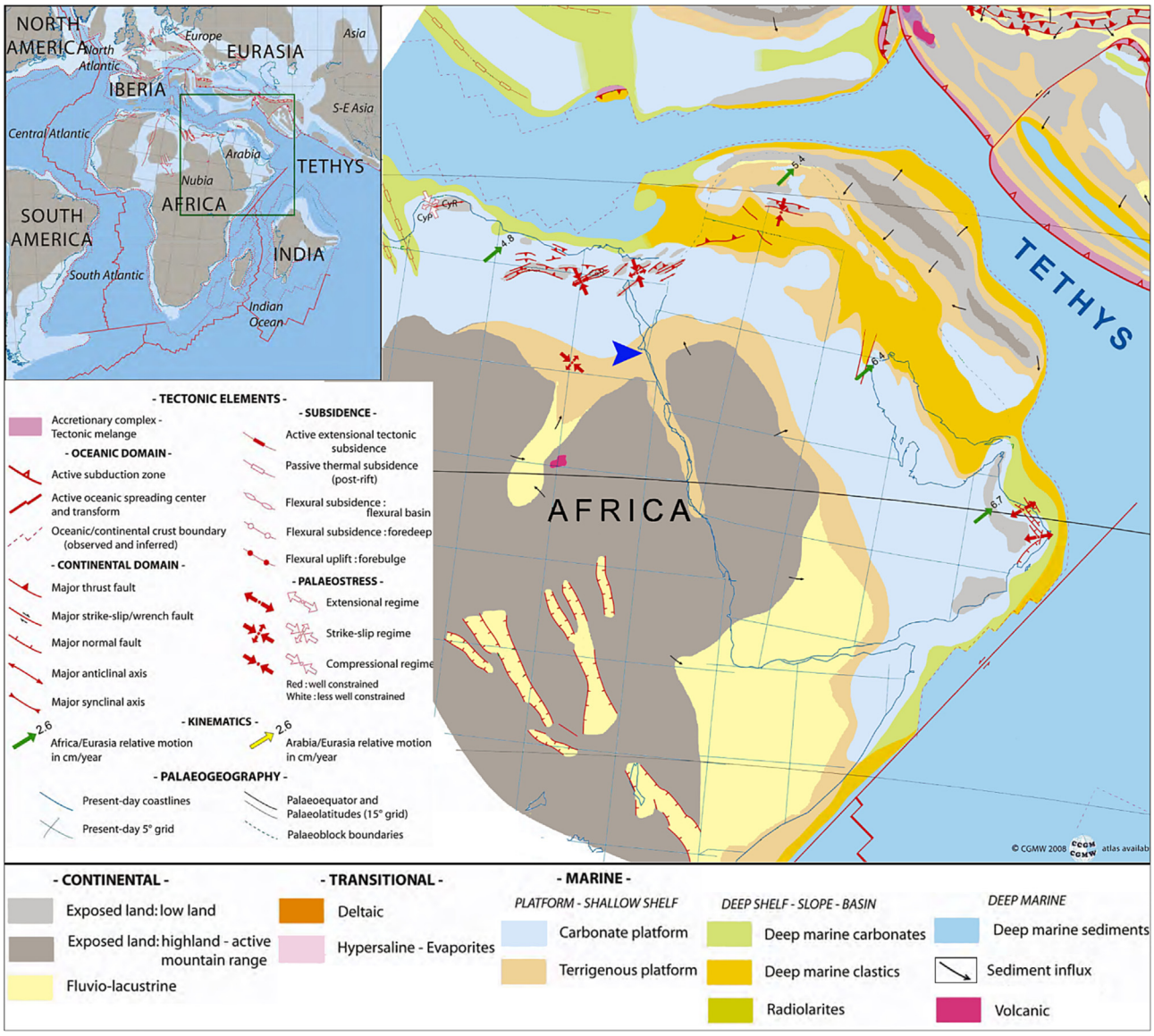

Fig. 1. A paleo-tectono-sedimentary map of the north African-Arabian Tethyan margin during the Latest Cretaceous (65.5–67.5 Ma; Barrier et al., 2008). The blue arrow indicates the location of the Quseir borehole in the present study. (For interpretation of the references to colour in this figure legend, the reader is referred to the web version of this article.)

tion from upper Dakhla Formation along with high organic carbon interval).

From the Campanian to the Eocene, a substantial transgressive phase occurred that resulted in rising sea-levels in Egypt, where the Tethyan Circumglobal Current (TCC) ran from east to west along the African-Arabian continental shelf (Abed, 2013). Due to the collision of the African-Arabian Plate with the intra-oceanic subduction of Eurasia, the first compressional event of the Syrian Arc inversion occurred that resulted in intra-plate paleo-highs in the northern to the northwestern part of the African-Arabian platform (Bevan and Moustafa, 2012; Abed, 2013; Fig. 1). Basin inversion, faulting, uplifting, and subsequent erosion began in the late Cretaceous and continued until the late Oligocene-Miocene period (Bevan and Moustafa, 2012). As a result, most of the eastern Mediterranean seafloor was made up of a series of topographic highs and lows (Guiraud and Bosworth, 1999; Guiraud et al., 2005; Abed, 2013). It is noteworthy that Khalil and McClay (2002 and 2009) conducted cross-section analyses of various sectors along the northwestern Red Sea margin, revealing a tilted pre-rift K-Pg sedimentary sequence with fault-related fold structures in the NE direction. The rift border fault system consists of multiple WNW- and NW-trending segments that bound northeast-dipping half-grabens, forming the Duwi accommodation zone (Fig. 2B).

3. Material and methods

3.1. Sampling

The organic-rich succession analyzed in this study was obtained from a core drilled by the Egyptian Mineral Resources Authority (EMRA) and sponsored by DanaGas© Egypt. The drilling site is located in the Quseir area, situated at the base of the Duwi Mountain along the Red Sea coast of Egypt (Figs. 1-2B). Two sampling strategies were employed. The first strategy involved collecting samples at 10 cm downcore intervals, and then combining 10 consecutive samples after thorough mixing into a bulk sample representing each 1 m interval. This approach was utilized for

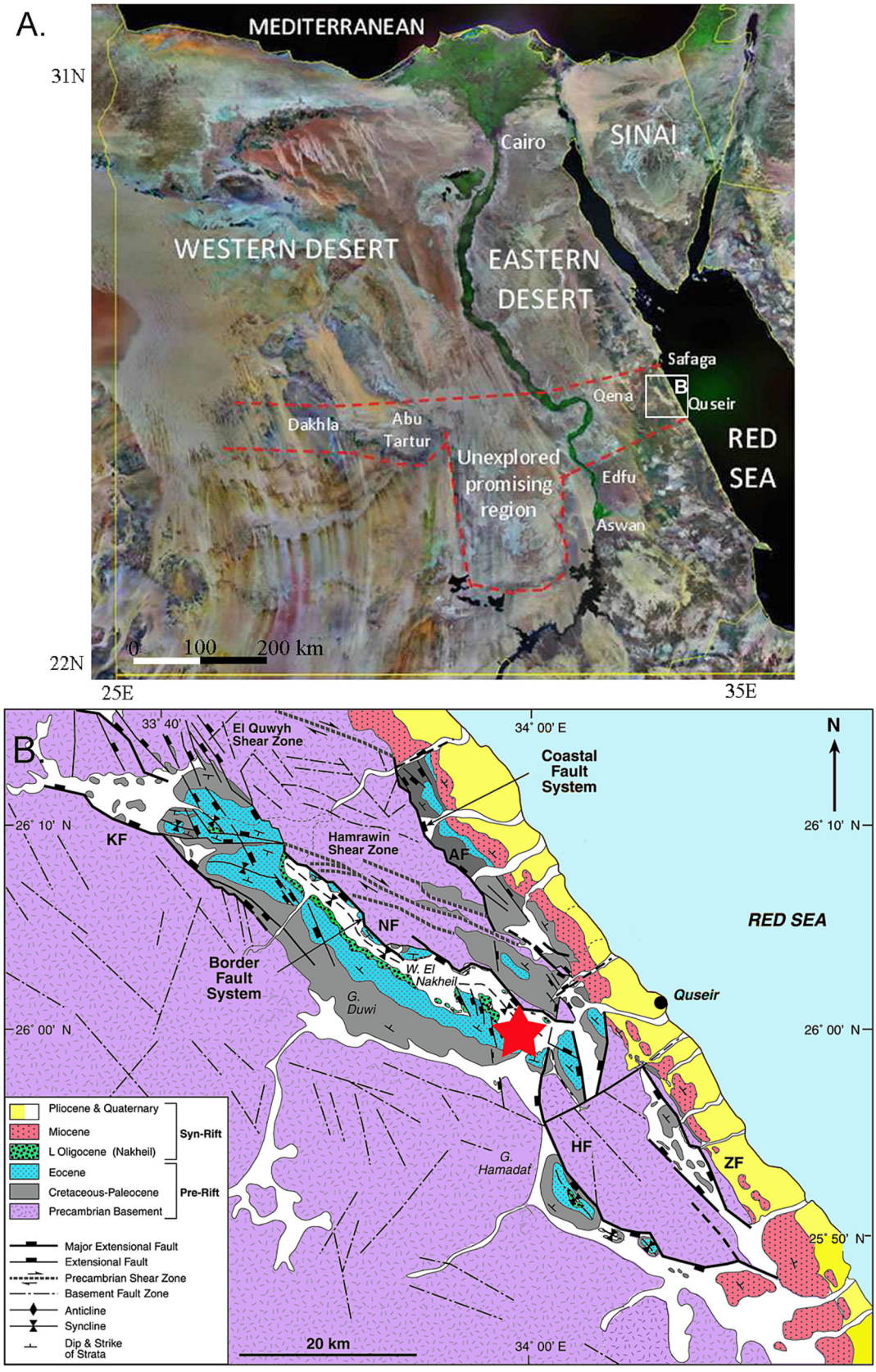

Fig. 2. (A) A satellite image shows the geographic distribution of the K-Pg organic-rich sedimentary succession in Egypt (El-Kammar, 2020). (B) A simplified geologic map of the northwestern Red Sea area (highlighted by a white square in "A") and the associated fault systems (Khalil and McClay, 2002). The location of the study core is indicated with a red star. It is worth noting that KF, NF and HF in (B) indicate the Kallahin, Nakheil, and Hamadat fault segments of the Border fault system, respectively. Additionally, AF and ZF represent the Anz and Zug El Bahar fault segments of the Coastal fault system, respectively. (For interpretation of the references to colour in this figure legend, the reader is referred to the web version of this article.)

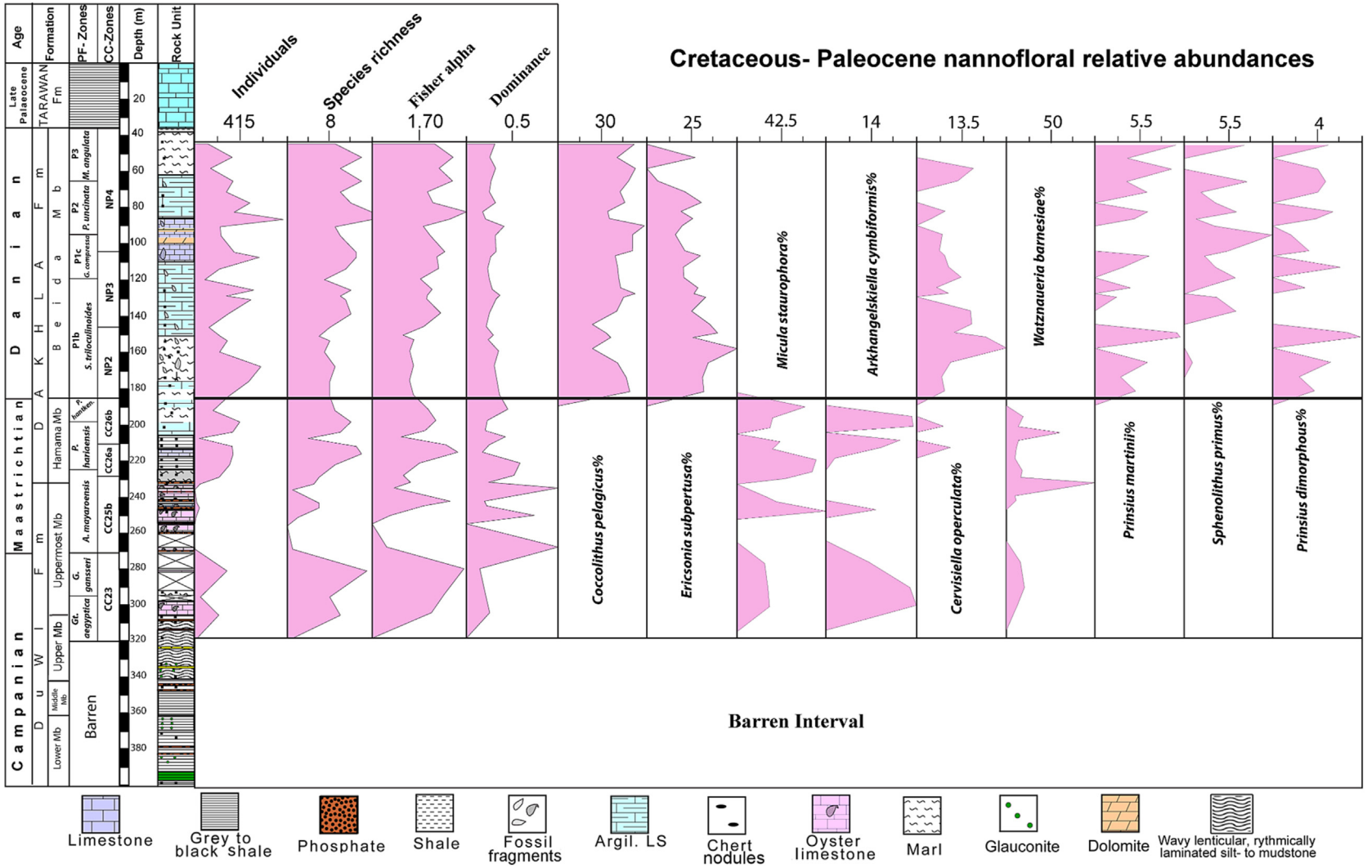

Fig. 3. Diversity indices and relative abundance of the most common calcareous nannofossil species recorded throughout the late Cretaceous to early Paleocene of the Quseir section. The lithology legend can be used for Figs. 3-5, 8, and 10.

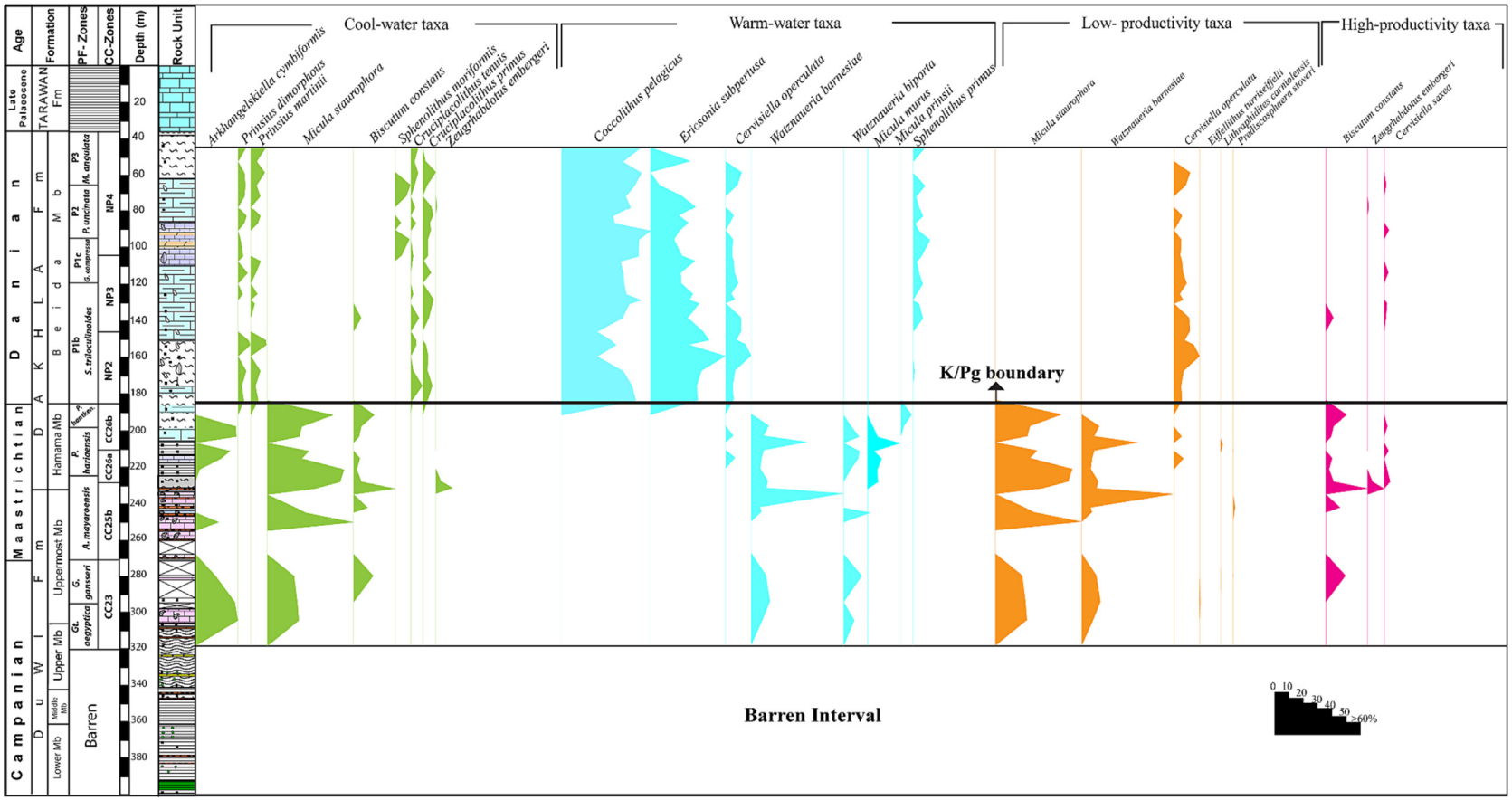

Fig. 4. Relative abundance of the most common indicator species of calcareous nannofossils during cool, warm, low productivity, and high productivity intervals recorded throughout the late Cretaceous to early Paleogene of the Quseir section.

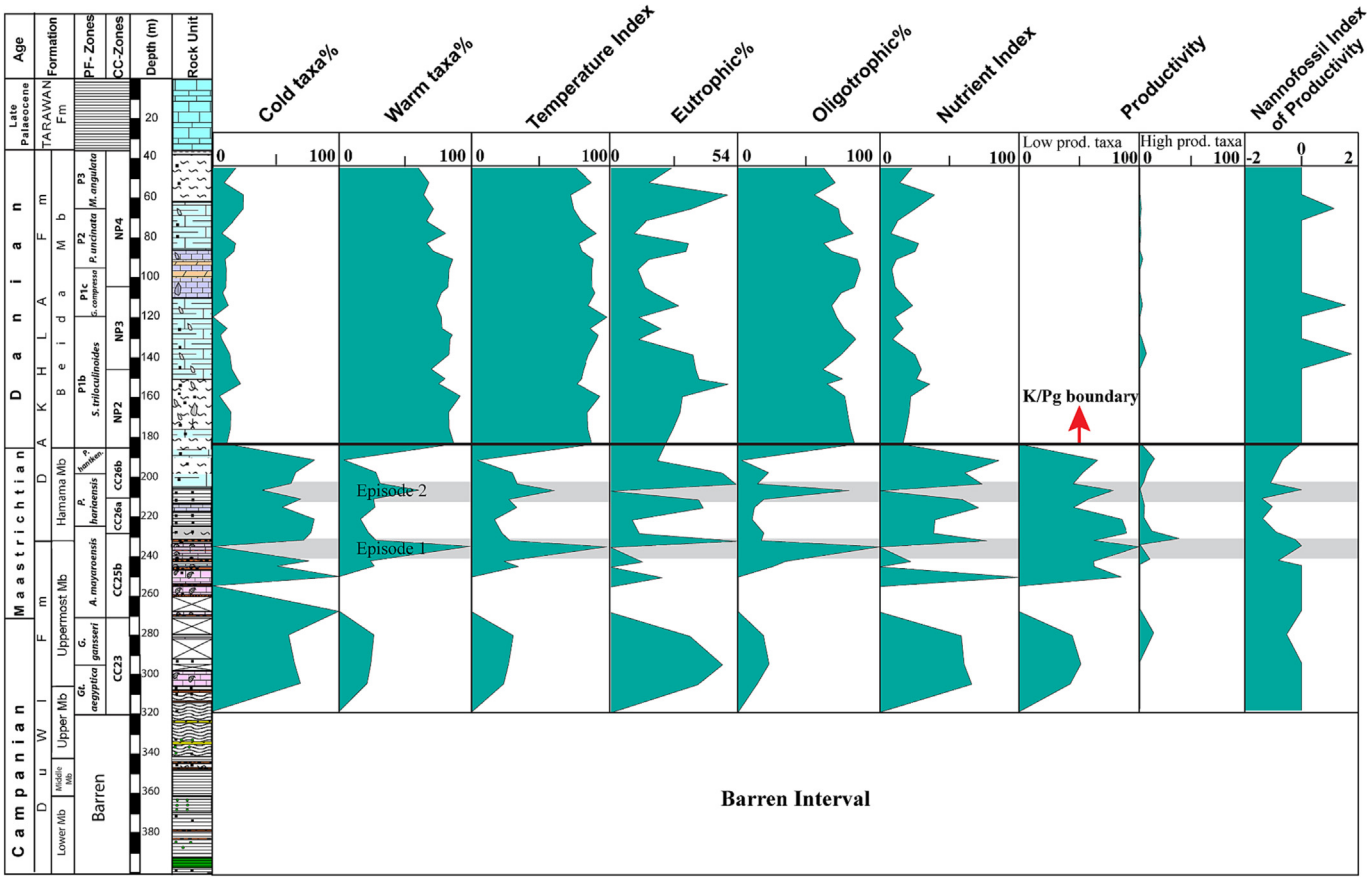

Fig. 5. Paleoclimatic and paleoecological indices of the late Cretaceous-early Paleocene strata in the Quseir section.

screening analyses of total organic carbon (TOC), Rock-Eval pyrolysis, and elemental analyses (data courtesy of DanaGas©). The second sampling strategy involved collecting individual samples from specific depths to monitor facies changes and important transitions. These samples were utilized for isotopes and calcareous nannofossil analyses.

3.2. TOC and Rock-Eval pyrolysis

The TOC content (wt%) and Rock-Eval pyrolysis data were obtained following the procedures outlined by El-Shafeiy et al. (2017) and conducted at StratoChem laboratories in Egypt. Briefly, the homogenized ground samples reacted with HCl to dissolve inorganic carbon and then combusted in a LECO C230 or EC-12 furnace to measure the resulted CO_2 using an infrared detector. For Rock-Eval pyrolysis, the sample material underwent isothermal heating at 300 °C, detecting the S1 free hydrocarbons using a flame ionization detector (FID). The temperature was increased to 600 °C to release additional hydrocarbons (S2), simulating the pyrolytic degradation of kerogen. The rock's hydrocarbon potential was determined after dividing S2 by the TOC and expressed as the hydrogen index (HI). The CO_2 released after cooling to ~ 400 °C is reported as S3.

3.3. Elemental analysis

Major and trace metal contributions were measured using the Inductively Coupled Plasma-Mass Spectrometry (ICP-MS) technique at ACME Laboratories in Vancouver, Canada (see El-Shafeiy et al., 2016; 2017 for details). In summary, the homogenized samples were dissolved using 4 ml HNO_3, 3 ml $HClO_4$, and 5 ml HF. The solution was then dried by heating it to 200 °C. The residue was dissolved in 5 ml of hot HNO_3. Each sample was then given 5 ml of a 4-ppm indium solution as an internal standard. Before each measurement, the nebulizer and spray chambers were washed for 3 minutes with the solution.

The chemical index of alteration (CIA) was estimated in the present work for shale and mudstone strata. CIA was calculated as molar amounts of $Al_2O_3 \times 100 / (Al_2O_3 + CaO^* + Na_2O + K_2O)$. CaO^* should represent the content in the silicate phase only (Nesbitt and Young, 1982), and therefore can be modified as CaO^* = mole CaO - mole $P_2O_5 \times 10/3$. If CaO^* remains higher than Na_2O, it can be assumed to correspond to Na_2O (McLennan, 1993). Moreover, the diagenetic K_2O can be corrected to each sample using the Al_2O_3–($CaO^* + Na_2O$)–K_2O [A–CN–K] ternary diagram (Fedo et al., 1995). Instead, corrected K_2O can be estimated using the method; $K_2O_{corrected} = [m \times Al_2O_3 + m \times (CaO^* + Na_2O)]/(1 - m)$, where m stands for the molar values of $[K_2O/(Al_2O_3 + CaO^* + Na_2O + K_2O)]$ of the parent rock (Panahi et al., 2000; Rieu et al., 2007). Thereafter, the calculated CIA values can be expressed as $CIA_{corrected}$. We limited ourselves to applying the CIA on strata with a considerable amount of terrigenous matter. Therefore, we did not include pure carbonate rocks in such computation. Additionally, the enrichment factor of trace elements such as Mo and U was estimated as

$$M_{EF} = (M/Al)_{Sample} / (M/Al)_{PAAS}$$

where M represents the relevant element and PAAS represents the post-Archean average shale (Taylor and Mclennan, 1985).

3.4. Stable isotope analysis

Stable isotope analysis of carbon and nitrogen was conducted in the stable isotope laboratory of the Institute of Geology and Geo-

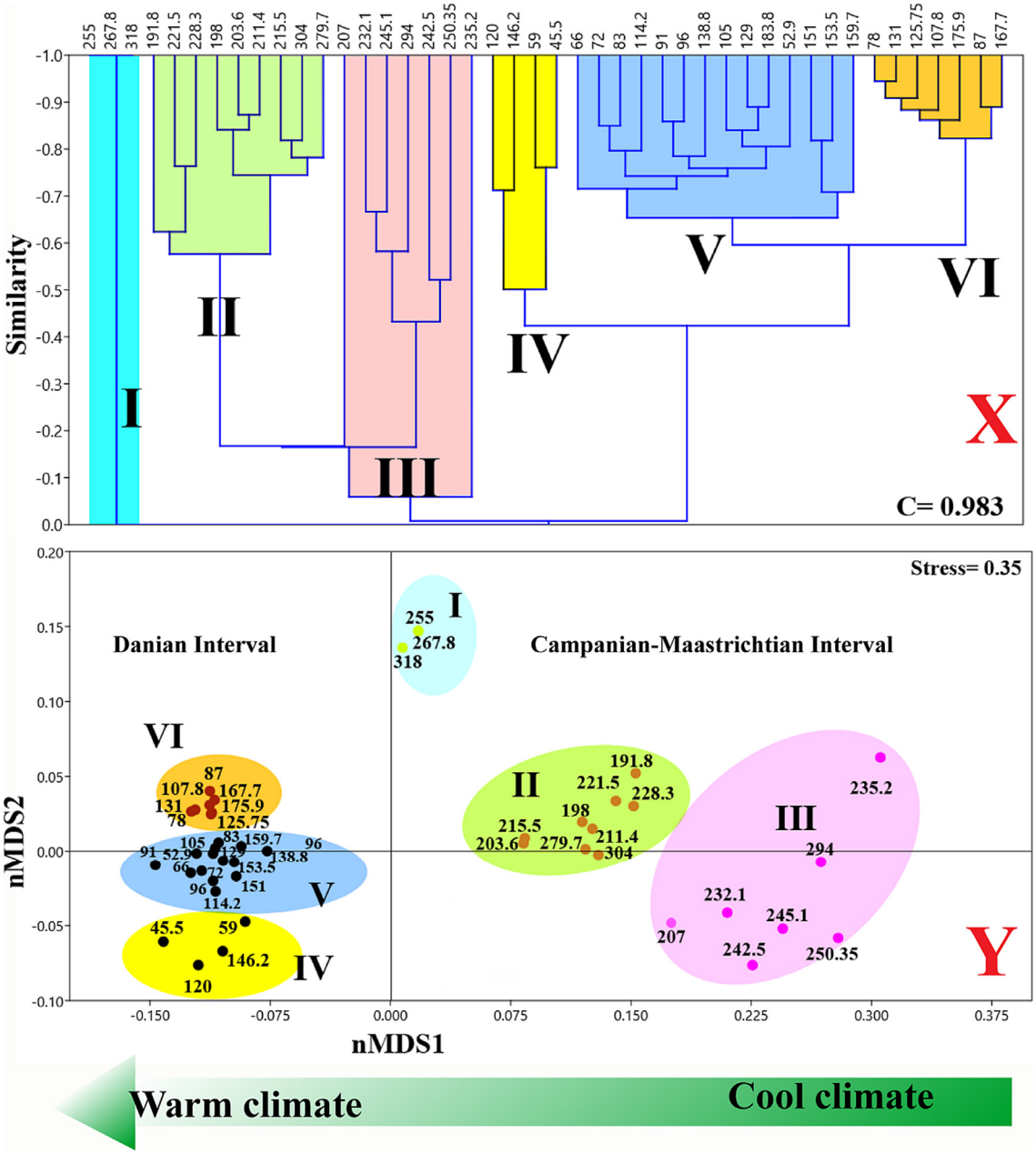

Fig. 6. Panel X represents Q-mode cluster analysis, and panel Y represents Q-mode nMDS analysis of calcareous nannofossil occurrences > 1 % using Raup-Crick similarity.

physics, Chinese Academy of Sciences (IGGCAS, Beijing). An elemental analyzer was linked to a Delta V Plus isotope ratio mass spectrometer (IRMS) via a ConFlo interface. The stable carbon and nitrogen isotope compositions were reported in per mil relative to VPDB and AIR, respectively, using the usual δ-notation.

The Cr reduction process was used to extract pyrite sulfur (Canfield et al., 1986). To accomplish so, 2–3 g of powdered material were heated for 2 h under a stream of nitrogen with roughly 20 ml of HCl and 40 ml of $CrCl_2$ solution, and the released H_2S was subsequently combined with excess $AgNO_3$ to produce Ag_2S precipitate. The sulfur isotope data were collected using a Thermo Fisher Scientific Delta V Plus IRMS coupled to a Flash elemental analyzer at the State Key Laboratory of Biogeology and Environmental Geology, China University of Geosciences in Wuhan. The Delta V Plus IRMS is linked to an elemental combustion system, and the sulfur isotope data were calibrated using three standards and represented relative to the VCDT in δ-notation.

3.5. Re-Os isotope analysis

The Re and Os isotope analysis methodology was adapted from Chu et al. (2015) and carried out in the Radiogenic Isotope Geochemistry Laboratory of the IGGCAS (Beijing). In summary, 0.5 g of powdered material was spiked with the appropriate proportions of a mixed ^{185}Re-^{190}Os spike. Using the Carius tube technique, samples were subsequently attacked by CrO_3-H_2SO_4 solution (Selby and Creaser, 2003) at 220 °C for 48 h (Shirey and Walker, 1995). Os was then extracted with CCl_4 from the CrO_3-H_2SO_4 solution and then back-extracted with 4 ml HBr (Cohen and Waters, 1996). Microdistillation was used to further purify Os (Birck et al., 1997). The refined Os was loaded onto high-purity platinum filaments and analyzed as OsO_3^- (Creaser et al., 1991) using a TRITON Plus thermal ionization mass spectrometer (TIMS) in a negative mode. Samples were measured in a peak-jumping mode using a single secondary electron multiplier (Chu et al., 2015). During the analytical sessions, an in-

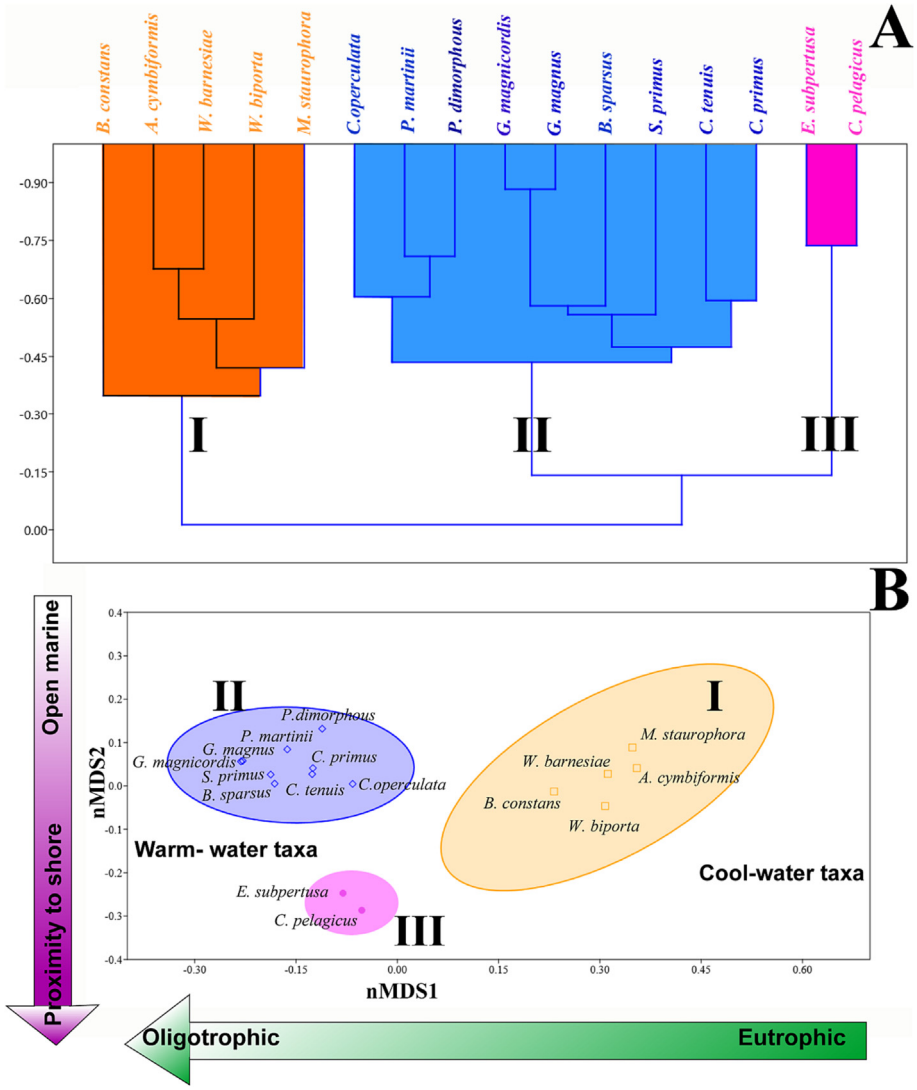

Fig. 7. Panel A represents R-mode cluster analysis, and panel B represents R-mode nMDS analysis of calcareous nannofossil occurrences > 1 % using Raup-Crick similarity.

house Johnson-Matthey standard of UMCP (University of Maryland, College Park) was used. This standard was measured, and the resulting average $^{187}Os/^{188}Os$ ratio was determined to be 0.1138 ± 0.0002 (2σ; n = 5). This measurement aligns with previous research findings (0.113791 ± 0.00015; Shirey and Walker, 1998).

After the reduction of Cr (VI) to Cr (III) using high-purity ethanol, the remaining Re in the solution was converted to ReO_4^- form and separated using a two-step anion-exchange chromatography method based on HCl–HNO_3 (Chu et al., 2015). Subsequently, the Re isotope composition was determined using a Thermo-Scientific Neptune multi-collector ICP-MS (MC-ICP-MS) in a static mode with Faraday Cups. To correct for Re isotope fractionation during the MC-ICP-MS measurements, a 10 ng/g Re standard solution ($^{187}Re/^{185}Re$ = 1.6738) was measured as a calibrator for every six samples. During this experiment, the total procedural blanks were determined to be 15 ± 5 pg for Re and 1 ± 0.5 pg for Os. The average value of $^{187}Os/^{188}Os$ for the blank was found to be 0.16 (n = 3). In most samples, the blank corrections accounted for less than 1 % of the measured values, rendering them negligible.

3.6. Micropaleontological analysis

A total of 60 sediment samples from the Quseir core section were investigated in-house, with about 1 g of bulk sediment used for calcareous nannofossil examinations. The technique for preparing smear slides followed Bown and Young (1998). The examination of calcareous nannofossil specimens utilized a 1000x magnification lens, cross-polarized light, and a gypsum plate to differentiate between closely similar taxa. For quantitative analysis, around 300 specimens were counted along a random path using a light microscope, ensuring a reliable statistical analysis (Fig. 3). Additionally, quick slide-skimming was conducted to identify any rare or marker species and their relative abundance (documented in Appendix 1).

Numerous calcareous nannofossil taxa were identified as indicators of varying sea-surface temperatures (Table 1) that were used to estimate paleotemperature changes within the studied section. Furthermore, based on their paleoecological preferences, calcareous nannofossils were classified into two groups (Fig. 4). The first group comprises warm-water indicator taxa that are typically found in low-latitude tropical environments while being absent in high-latitude regions. The second group consists of cool-water indicator taxa that were abundant in high-latitude sites during the Cretaceous to the early Paleocene. To better illustrate the response of each species to the temperature gradient, they are presented as distinct entities in Table 1. Eshet and Almogi-Labin (1996) conducted statistical analyses that identified two groups of taxa serving as indicators of paleo-productivity, namely, low-productivity and high-productivity

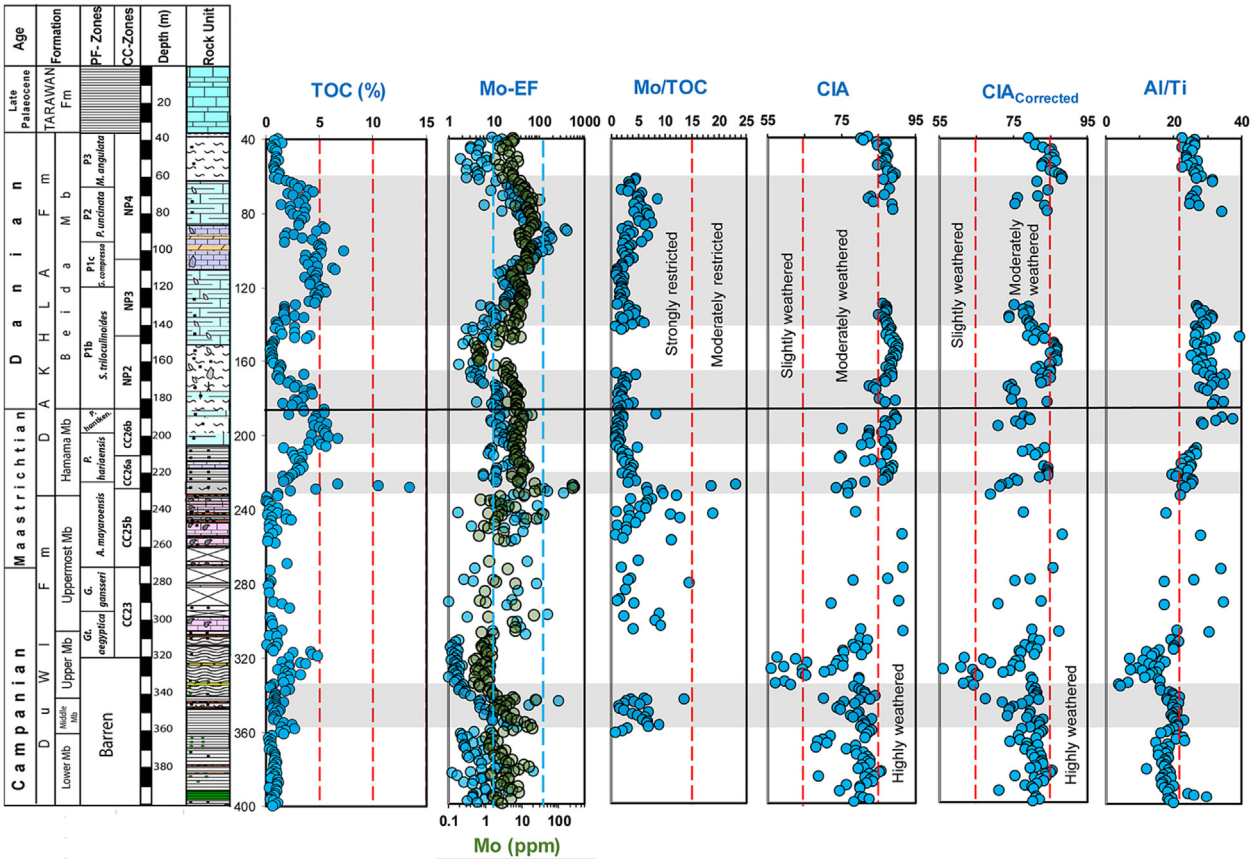

Fig. 8. Distribution profile of TOC%, Mo content (ppm) and enrichment factor (Mo_{EF}), chemical index of alteration (CIA), corrected chemical index of alteration ($CIA_{Corrected}$), and Al/Ti ratio for the different rock units in the Quseir section. Note that the red dashed line in the Al/Ti profile represents the upper continental crust ratio, while the faint blue dashed lines in the Mo_{EF} profile represent enrichment thresholds of 10 and 100. (For interpretation of the references to colour in this figure legend, the reader is referred to the web version of this article.)

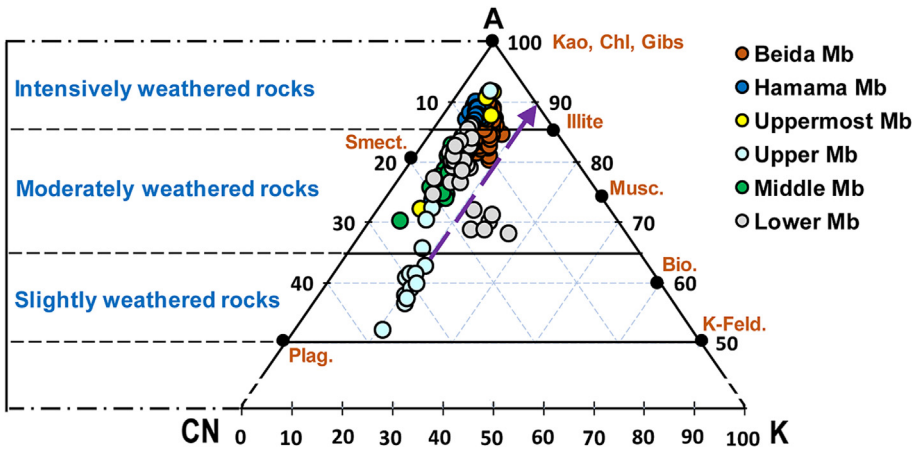

Fig. 9. A-CN-K diagram plot for the data from the studied intervals in the Quseir section, based on the method by Nesbitt and Young (1982). CN represents (CaO^*+Na_2O), where CaO^* denotes the CaO present in the silicate fraction, and K represents K_2O (both in molar proportions). Plag. stands for plagioclase, Smect. for smectite, Kao for kaolinite, Gibs for gibbsite, Chl for chlorite, Musc. for muscovite, and Bio. for biotite. The dashed violet arrow indicates the weathering trend parallel to the A-CN line. (For interpretation of the references to colour in this figure legend, the reader is referred to the web version of this article.)

indicators. The relative abundance of species characteristic to trophic states (Eutrophic vs. Oligotrophic) and the species indicating paleoproductivity are computed and categorized in Table 1. Additionally, paleoecological indices such as the Temperature Index (TI), the Nannofossil Index of Productivity (NIP), and the Nutrient Index (NI) have been calculated (Fig. 5).

In addition, samples obtained during the investigation were analyzed for planktonic foraminifera as another approach to establishing well-defined chronostratigraphic boundaries for the Campanian-Maastrichtian and Maastrichtian-Danian periods. Biostratigraphic zonation followed the established frameworks of Huber et al. (2008) and Li et al. (1999) for the Cretaceous, as well

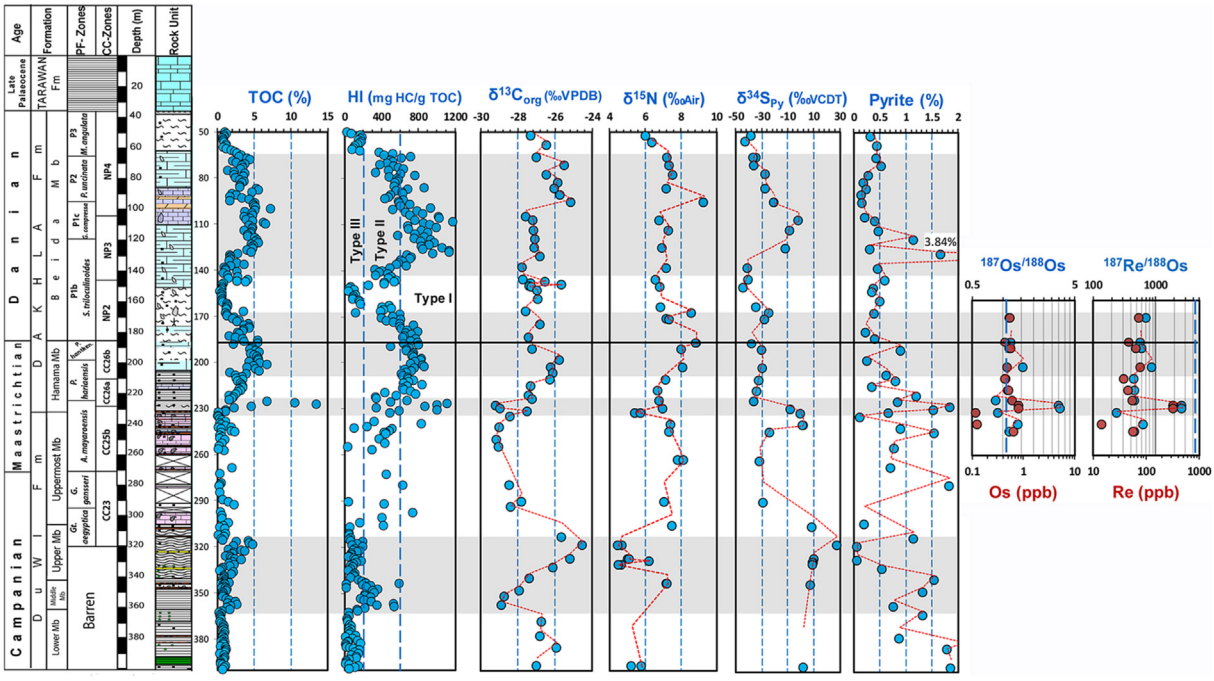

Fig. 10. Secular distribution of TOC%, hydrogen index (HI), $\delta^{13}C$ for bulk organic matter, $\delta^{15}N$ for bulk sediment, pyrite $\delta^{34}S$, and pyrite content (%), as well as $^{178}Os/^{188}Os$ and $^{178}Re/^{188}Os$ ratios along with Os and Re contents. The data of TOC% and HI are used after El-Shafeiy et al. (2017), whereas pyrite contents are used after El-Shafeiy (2012). Blue dashed lines in the HI profile indicate threshold values for different kerogen types, and the blue dashed line in the $^{178}Os/^{188}Os$ and $^{178}Re/^{188}Os$ profiles represents the average ratios in seawater (1.06 and 4270, respectively; Peucker-Ehrenbrink and Ravizza, 2000). (For interpretation of the references to colour in this figure legend, the reader is referred to the web version of this article.)

as Wade et al. (2011) for the Paleogene. As part of the future research scope, a comprehensive biostratigraphic study integrating planktonic foraminifera and nannofossil assemblages from the cored borehole can be achived in the future.

3.7. Statistical analysis of calcareous nannofossil

To enhance the statistical analyses, the occurrence data of the species-sample matrix was transformed into a percentage abundance. The dataset (Appendix 1) was subjected to constrained clustering Q and R-modes using the Raup-Crick similarity index to identify the calcareous nannofossil assemblages. We focused on species occurrences with relative abundances higher than 1 % to ensure robust analysis. To visualize the relationships among the identified assemblages, Non-Metric Multidimensional Scaling (NMDS) was employed, utilizing the Raup-Crick similarity coefficient based on the methods described by Legendre and Legendre (1998) and Hammer and Harper (2006). Biplot charts were generated to display the first two axes, which represent the most significant eigenvalue proportions in the NMDS result. All correlations were tested for significance at a level of $p < 0.01$. The nature of the identified assemblages was evaluated using diversity indices including species richness, dominance, and Fisher's alpha. These indices were generated using the Paleontological Statistics Toolkit (PAST), version 4.08, as described by Hammer et al. (2001).

4. Results

4.1. Calcareous nannofossil assemblage

The calcareous nannofossil assemblage in the core at investigated intervals consisted of 57 species in a moderate to well-preserved state. Quantitative analysis revealed a mixture of calcareous nannofossil assemblages typical of low and high latitudes during the Late Cretaceous, aligning with previous results of Thierstein (1981) regarding assemblages at similar latitudes. Notably, the calcareous nannofossil assemblages were absent in the Lower and Middle members, and the lower part of the Upper Member of the Campanian Duwi Formation. However, *Micula staurophora* exhibited fluctuations throughout the late Campanian-Maastrichtian interval, reaching ~ 85% of the total calcareous nannofossil assemblage in the Uppermost part of the Duwi Formation (Fig. 3). Additionally, *Arkhangelskiella cymbiformis* makes up to ~ 31% of the total calcareous nannofossil assemblage (Fig. 3), where it displays a remarkably similar abundance pattern at the intervals with *M. staurophora*. In the lower part of the Maastrichtian Dakhla Formation, *Watznaueria barnesiae* constituted ~ 60% of the total assemblage, showing an inverse pattern to *M. staurophora* and *A. cymbiformis*. At the base of the Danian Dakhla Formation, *Cervisiella operculata* accounts for ~ 17% of the total assemblage, decreasing until the beginning of the NP4 Zone before increasing again (Fig. 3).

The quantitative analysis of the Paleocene (Danian) calcareous nannofossil species showed that some taxa constitute over 70% of the total assemblage. *Coccolithus pelagicus* emerged as the dominant species, followed by *Ericsonia subpertusa*, and exhibited fluctuations throughout the interval, with a relative abundance reaching ~ 60% at a depth of 91 m (Fig. 3). *Ericsonia subpertusa* was the second most prevalent species, with a distinct peak of ~ 50% observed in the lower part of the Beida Member. *Sphenolithus primus*, *Prinsius martini*, and *Prinsius dimorphus* showed similar fluctuation patterns throughout the Danian interval, with relative abundances of 11%, 10.5%, and 8%, respectively (Fig. 3). The highest relative abundance of *Prinsius* spp. is observed at the base of the Danian interval (top of NP2), while the relative abundance peak of *S. primus* is found at the lower part of the NP4 Zone (Fig. 3).

The diversity indices below the K-Pg differed significantly from those above the transition. During the Campanian period, the

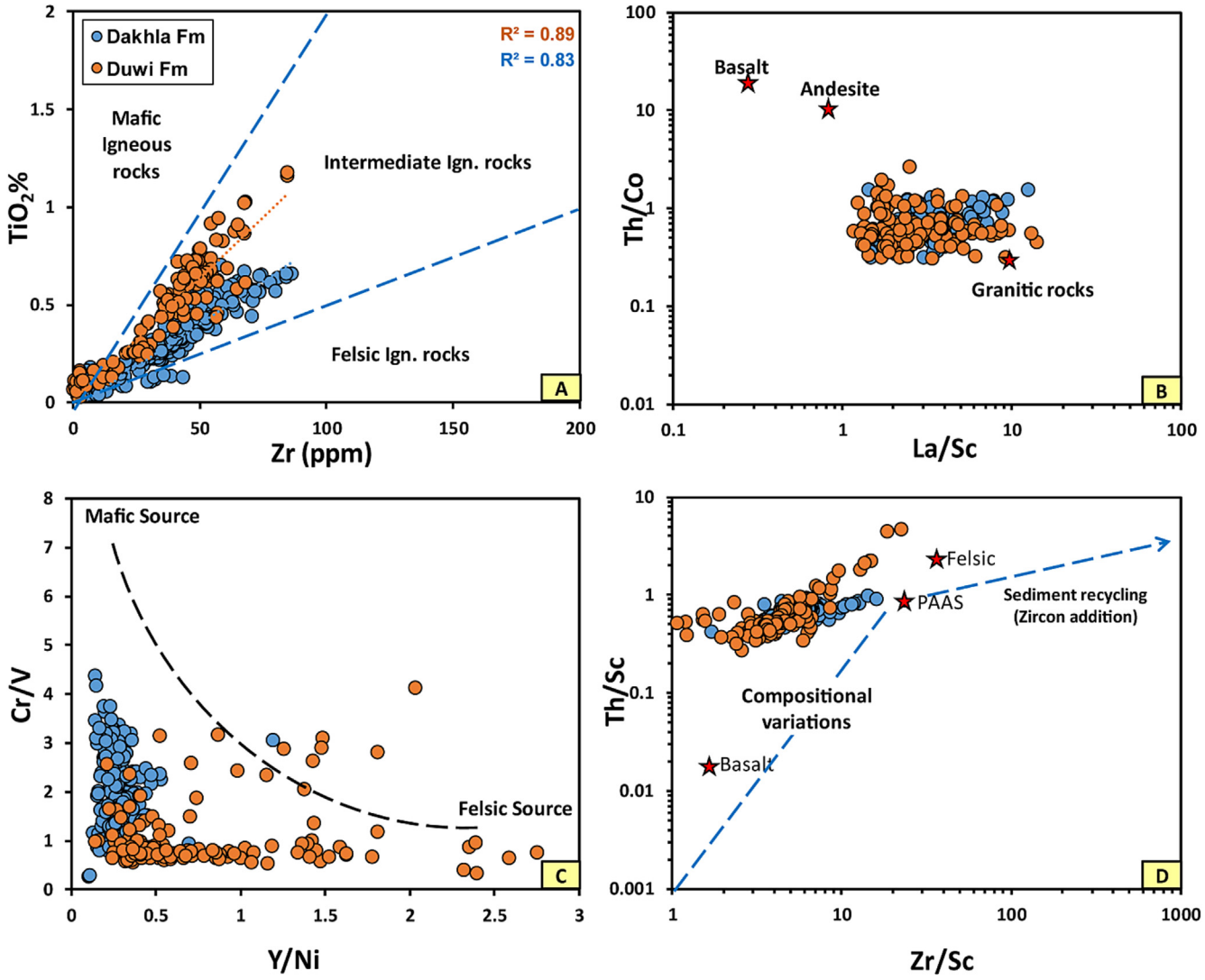

Fig. 11. Discrimination diagrams demonstrating sedimentary provenance (A-C) and the influence of sediment recycling (D). Panel A shows the TiO_2 vs. Zr diagram (Hayashi et al., 1997), Panel B shows the Th/Co vs. La/Sc diagram (Cullers, 2002), Panel C shows the Cr/V vs. Y/Ni diagram (Hiscott, 1984), and Panel D shows the Th/Sc vs. Zr/Sc diagram (McLennan et al., 1993).

Uppermost Member of the Duwi Formation exhibited higher calcareous nannofossil abundance, species richness, and Fisher alpha indices compared to the Upper Member (Fig. 3). The highest calcareous nannofossil abundance was recorded in the Uppermost Member at depth 279.7 m; here species richness, Fisher alpha, and Dominance are 15, 3.31, and 0.15, respectively (Fig. 3). Conversely, the top part of the Uppermost Member showed lower abundance, species richness, and Fisher alpha, but higher dominance index, primarily due to the high relative abundance of a few species such as *A. cymbiformis*, *M. staurophora*, and *W. barnesiae* (Fig. 3). The Hamama Member of the Dakhla Formation exhibited fluctuating high diversity indices and a low dominance index. At 215.5 m depth, the calcareous nannofossil abundance, species richness, and fisher alpha are 355, 14, and 3.1, respectively, whereas the dominance index showed the lowest value of 0.34 (Fig. 3).

Above the K-Pg transition, the diversity indices fluctuated throughout the entire Danian interval. The sample at a depth of 87 m within the NP4 Zone displayed the highest calcareous nannofossil abundance, species richness, and Fisher alpha, with values of 830, 16, and 2.8, respectively, while the dominance index was 0.35 (Fig. 3). Conversely, the lowest diversity indices and high dominance index were observed at a depth of 120 m within the NP3 Zone, with values of 95, 7, and 1.7, respectively, and a dominance index of 0.42 (Fig. 3).

4.2. Paleoecological analysis of the calcareous nannofossil

The quantitative analysis of the calcareous nannofossil assemblage spanning the Late Cretaceous (Campanian-Maastrichtian) to the early Paleocene (Danian) periods reveals significant variations in climatic conditions. The presence of *A. cymbiformis* and *M. staurophora*, the most prominent indicators of cool sea-surface water in this study, provides evidence of prevailing cool climatic conditions during the late Cretaceous (Fig. 4). These species constitute a substantial proportion of the cool water species, while other high-latitude taxa such as *Prediscosphaera stoveri*, *Tranolithus orionatus*, *Lithraphidites* spp., and *Biscutum constans* are present in negligible quantities. The Late Cretaceous period experienced a relatively cool climate, punctuated by two noticeable warming episodes. The first episode occurred in the upper part of the CC25b Zone, while the second episode was observed in the lower part of the CC26a Zone (Fig. 5). These warming events are reflected by the high relative abundance of *Watznaueria barnesiae*, *Lithraphi-*

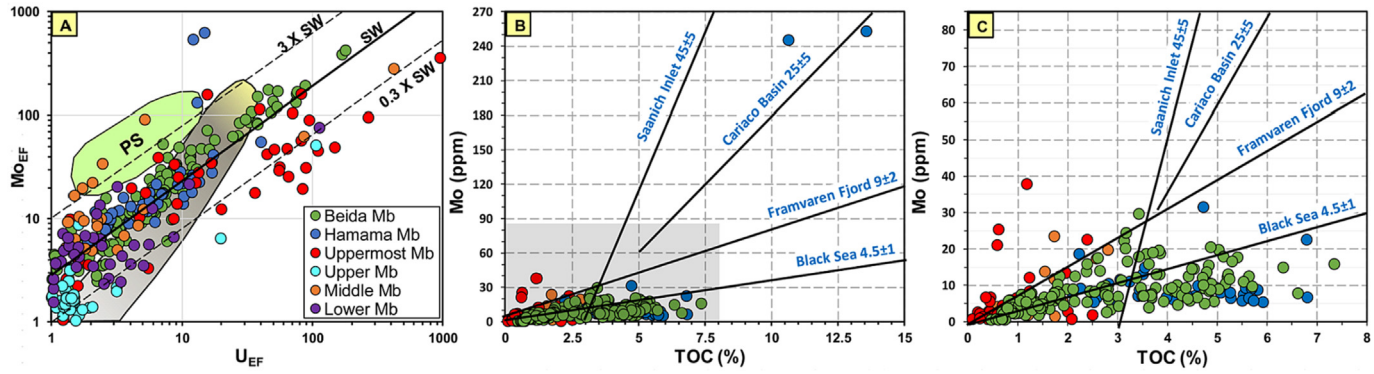

Fig. 12. (A) Cross-plot of Mo vs. U enrichments for different intervals in the studied section. PS represents particulate shuttles (Algeo and Tribovillard, 2009). (B) Covariation diagram of Mo vs. TOC% (Algeo and Lyons, 2006) for samples from the studied Quseir section. (C) represents the grey-shaded rectangle in (B).

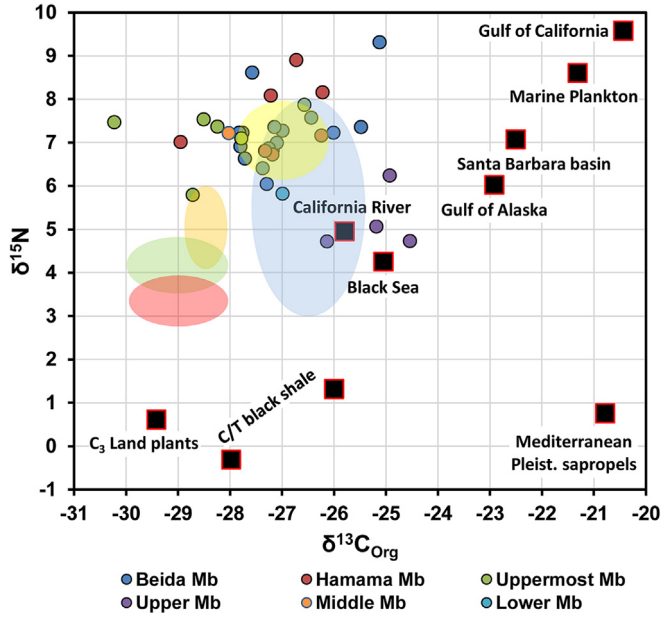

Fig. 13. Cross-plot of $\delta^{15}N$ vs. $\delta^{13}C_{Org}$ for the intervals in the Quseir section, providing information about source of the organic matter. Black squares represent data from Meyers (1997). The red, green, orange, and yellow ellipsoids represent the zones of samples from the top Phosphate member, the lower Oil Shale member, the middle-upper Oil Shale member, and the Marl member, respectively, of the Negev section (Schneider-Mor et al., 2012). Additionally, the blue ellipsoid signifies the zone of samples from the El Kef and Aïn Settara sections in Tunisia (Sepúlveda et al., 2019). (For interpretation of the references to colour in this figure legend, the reader is referred to the web version of this article.)

dites quadratus, and *Ceratolithoides kamptneri* (Fig. 5). During these warming episodes, cool-water species declined, particularly during the first episode, which witnessed a sudden drop in species richness (Figs. 4-5). This drop was significant, with species richness decreasing from ~ 5–7 species per sample before the warming event to only 1–2 species per sample during the event (Figs. 4-5). Moreover, most species in this interval temporarily disappeared, except for *M. staurophora* and *W. barnesiae*, which remained present in significant numbers, accounting for ~ 28% and up to 100% of the whole calcareous nannofossil assemblage, respectively. The high abundance of these taxa suggests the presence of stressful marine conditions, which could be indicative of a very shallow marine environment associated with low-productivity conditions. These taxa can be regarded as opportunistic species, as noted in previous studies (e.g., Tantawy, 2003). In contrast to the Late Cretaceous period, the Danian was characterized by a dominance of warm-water calcareous nannofossils indicatives at the expense of cool-water taxa (Fig. 5). This is evident from the high relative abundance of the warm-water indicator species such as *Coccolithus pelagicus* and *Ericsonia subpertusa* (Fig. 4). The TI indicates clearly that warm conditions were prevalent during the Danian interval (Fig. 5).

Regarding the paleo-productivity, low-productivity taxa are dominated below the K-Pg transition. They exhibited fluctuations throughout the Late Cretaceous interval and reached the maximum (100%) at a depth of 235.2 m (Fig. 5). Instead, sporadic occurrences of high-productivity taxa were observed, with the highest value (38%) recorded at a depth of 232 m (Fig. 5). During the Danian period, the low-productivity taxa diminished, while the high-productivity taxa were recorded sporadically, reaching their highest value (6%) at a depth of 138.8 m. These findings align well with the results of the Nannoplankton Index of Productivity (Fig. 5).

Based on the affinities of the calcareous nannofossils, the trophic state could be classified into two categories: oligotrophic and eutrophic. During the Late Cretaceous of the Quseir section, the relative abundance of calcareous nannofossils represents either the eutrophic or oligotrophic group that fluctuated significantly throughout the interval (Fig. 5). The eutrophic percentage was high during the latest Campanian time, reaching up to 52%, while the oligotrophic percentage extends up to 24% (Fig. 5). However, the Maastrichtian time displays a wavered pattern, where the eutrophic state and NI dominate except for the two episodes 1 and 2, which indicated an oligotrophic state (Fig. 5). During the Danian time, overall oligotrophic conditions were dominated, reaching up to 86% at a depth of 96 m, whereas eutrophic conditions peaked at 34% at a depth of 154 m (Fig. 5).

The cluster and nMDS analyses conducted on the Q-mode (samples) reveal six distinct clusters labeled I, II, III, IV, V, and VI (Fig. 6). Cluster I comprises three samples characterized by the absence or scarcity of calcareous nannofossil content. The nMDS analysis shows a clear pattern with significant correlation coefficients among these samples. Cluster II consists of nine samples, except for the 279.7 m and 304 m samples, which exhibit a high occurrence of calcareous nannofossils during the Maastrichtian interval. The nMDS analysis confirms a strong correlation among this group, aligning with the cluster analysis results. Cluster III comprises seven samples, excluding the 235.2 m sample, and is characterized by notably low species abundance and diversity. On the nMDS biplot, clusters I to III are positioned on the positive side (Fig. 6), representing late Campanian-Maastrichtian samples.

Cluster IV consists of four samples located in the lower negative quadrant on the left side of the nMDS chart (Fig. 6). These samples exhibit moderate species abundance and richness (Fig. 3). Cluster V includes 14 samples with high species abundance and diversity,

Table 1
The paleoecological preferences of some calcareous nannofossil indicators according to the following references, 1-Van Simaeys et al. (2004), 2-Garecka (2012), 3-Wei and Wise (1990), 4-Faris et al. (2017), 5-Thierstein (1981), 6-Roth and Bowdler (1981), 7-Roth and Krumbach (1986), 8-Pospichal and Wise Jr (1990), 9-Shafik (1990), 10-Thibault and Gardin (2006), 11-Roth (1978), 12-Perch-Nielsen (1979), 13-Hallock (1987), 14-Gibbs et al. (2006), 15-Huber and Watkins (1992), 16-Watkins (1992), 17-Erba (1992), 18-Williams and Bralower (1995), 19-Eshet and Almogi-Labin (1996), 20-Perch-Nielsen (1985), 21-Bartol et al. (2008), 22-Persico & Villa (2004), 23-Wei et al. (1992), 24-Lees (2002), 25-Pospichal (1996), 26-Thierstein (1976), 27-Watkins et al. (1996), 28-Bralower (2002), 29-Firth and Wise Jr (1992), 30-Aubry (1992), 31- Monechi et al. (2000).

Species	Warm	Cold	Eutrophic	Oligotrophic	High productivity	Low productivity	References
Pontosphaera plana	■						1, 2
Coccolithus pelagicus	■			■			3, 28
Ericsonia subpertusa	■			■			3, 4, 28
Cervisiella operculata	■		■				5,6,7,8,9
Micula murus	■						10
Watznaueria barnesiae	■			■		■	8, 11,12,13, 15, 16, 17, 18, 19
Watznaueria biporta	■						
Sphenolithus primus	■			■			3, 20
Braarudosphaera bigelowii	■		■				21, 22
Ceratolithoides kamptneri	■						5
Cervisiella saxea	■		■		■		5, 19
Chiasmolithus danicus		■					3, 22, 23
Tranolithus orionatus		■					24
Ellipsolithus macellus		■					24
Lithraphidites quadratus		■					10, 19
Lithraphidites carniolensis		■		■		■	
Biscutum constans		■	■		■		17, 19, 24
Sphenolithus moriformis		■		■			23, 28, 30, 31
Prinsius martinii		■	■				3, 8, 28, 29
Prinsius dimorphous		■	■				
Arkhangelskiella cymbiformis		■	■				12, 19
Micula staurophora		■				■	24, 25
Eiffellithus turriseiffelii		■		■			5, 9, 16, 24
Eiffellithus gorkae				■			
Lucianorhabdus cayeuxii		■					26
Zeugrhabdotus embergeri		■	■		■		5, 6, 7, 17, 18, 24
Cribrocorona gallica		■					8
Placozygus sigmoides		■					8
Reinhardites levis		■					12, 10
Broinsonia enormis		■					24, 27
Prediscosphaera stoveri		■		■		■	19
Cruciplacolithus tenuis		■	■				12, 24
Cruciplacolithus primus		■	■				19, 25
Cruciplacolithus edwardsii			■				18, 24
Neochiastozygus modestus			■				14

positioned around the lower negative side of the nMDS 1 axis (Fig. 6X and Y). Cluster VI comprises seven samples strongly correlated with each other, as indicated on the nMDS biplot (Fig. 6X and Y). These samples demonstrate the highest species abundance and diversity throughout the succession (Fig. 3). Clusters IV to VI, located on the left of the nMDS, represent the Danian interval (Fig. 6).

The R-mode analysis of the cluster and nMDS data reveals three clusters (Fig. 7A and B). Cluster I discriminates five calcareous nannofossil taxa based on their relative abundance and affinities, namely *A. cymbiformis*, *B. constans*, *W. barnesiae*, *M. staurophora*, and *Watznaueria biporta*. This cluster aligns with the group I obtained from the nMDS data, where this calcareous nannofossil assemblage is positioned on the right (positive) side, resembling the Cretaceous samples in the Q-mode analysis. Cluster II represents nine calcareous nannofossil taxa, including *Cruciplacolithus primus*, *Cruciplacolithus tenuis*, *Cervisiella operculata*, *Prinsius martinii*, *Prinsius dimorphus*, *Gomphiolithus magnus*, *Gomphiolithus magnicordis*, *Sphenolithus prmus*, and *Biantholithus sparsus*. Cluster III is defined by the two most abundant Danian taxa, *C. pelagicus* and *E. subpertusus*. The nMDS biplot illustrates that groups II and III are positioned on the left (negative) side of the chart, showing similarities with the Q-mode analysis of the Danian interval.

The Q-mode of the nMDS data discriminates the Quseir section into warm and cool intervals (Fig. 6Y). The Campanian-Maastrichtian samples displayed on the positive side of the plot indicate a cool climatic condition, and include taxa such as *A. cymbiformis*, *M. staurophora*, *W. barnesiae*, *W. biporta*, and *B. constans* (Fig. 7B). Furthermore, these taxa show an increase towards the right side of the positive eigenvalues, suggesting eutrophic conditions (Fig. 7B and Table 1). Conversely, the Danian samples placed on the negative side represent a warm climatic episode. The negative left side is dominated by warm water-tolerant taxa, including *C. pelagicus*, *E. subpertusus*, *P. martini*, *P. dimorphus*, *C. primus*, *C. tenuis*, *B. sparsus*, *G. magnus*, and *G. magnicordis* that indicate an oligotrophic condition based on their enrichment status (Fig. 7B).

4.3. Redox-sensitive metals

Redox-sensitive elements explored in this study (Figs. 8 and 12) show that the secular distribution of Mo and Mo_{EF}, which indicate enrichment relative to PAAS, has a comparable trend to that of the TOC and HI profiles (Fig. 8). In the Upper Member, Mo and Mo_{EF} values reach a minimum (as low as 1.2 ppm and ~ 1, respectively), while they peak during the lowermost Dakhla TOC peak (reaching

as high as 253 ppm and ~ 400, respectively; Fig. 8). Moreover, the Mo contents and enrichment factors in the current study are consistent with those previously reported in the Maastrichtian strata of the study area (e.g., Fathy et al., 2023a).

4.4. Chemical index of alteration (CIA)

The CIA values of the Quseir section (Fig. 8) exhibit significantly lower values in the Duwi Formation, ranging from 56.3 to 91.8 (averaged 77.4), compared to the Dakhla Formation, which ranges from 73.7 to 90.5 (averaged 86.4). Similarly, the Al/Ti ratio in the Duwi Formation ranges from 4.0 to 34.5 (averaged 18.4), which is significantly lower than the Al/Ti values in the Dakhla Formation, ranging from 19.8 to 39.7 (averaged 27.9; Fig. 8). On the A-CN-K triangular plot (Fig. 9), most of the samples from the Duwi members are located between the slightly weathered rock field (Upper Member) and the moderately weathered rock field (Lower, Middle, and Uppermost members; Figs. 8-9). Conversely, the samples from the Dakhla Formation are situated sporadically in the moderately, but mainly in the intensively weathered rock fields (Figs. 8-9).

4.5. Organic matter characteristics and stable isotopes

The Duwi Formation displays TOC content ranging from 0.25% to 5.5%, with an average of 1.1%. In contrast, the Dakhla Formation exhibits two distinct organic-rich cycles, with the highest content peaking at ~ 4–5 m at the base of the lowermost cycle, reaching up to 14% and averaging 7.8% organic carbon content (Fig. 10). The kerogen types in the Quseir section were determined based on the HI values (Fig. 10). The Lower and Upper members contain terrigenous Type-III kerogen, while a significant portion of the Dakhla Formation as well as the Middle and Uppermost Duwi members exhibit mixed marine Type-II kerogen. A significant portion of the Hamama and Beida members, along with the TOC peak in the lowermost Hamama Member, are characterized by aquatic algal Type-I kerogen in the studied Quseir section.

In the Duwi Formation, the $\delta^{13}C_{Org}$ values ranged from −29.1‰ to −24.5‰ (Fig. 10). A positive carbon isotope excursion was detected during the Upper Member, reaching a maximum value of −24.4‰. Additionally, a negative carbon isotope excursion of a magnitude −2‰ (with a minimum of −29.2‰) was observed at the lower TOC peak of the Dakhla Formation (Fig. 10). Moving upwards, the $\delta^{13}C_{Org}$ values returned to heavier values in the remaining Upper Cretaceous strata (Fig. 10). Around the K-Pg transition, a negative shift was noted, reaching a minimum value of −27.5‰, with a magnitude of ~ -1.8‰ (Fig. 10). The remainder of the Beida Member is characterized by similar values of normal marine organic matter.

The $\delta^{15}N$ data exhibit a range of 4.7‰ to 7.8‰ in the Duwi Formation and 5.4‰ to 9.3‰ in the Dakhla Formation (Fig. 10). In the Duwi Formation, the Upper Member displays isotopically depleted values, while isotopically enriched values are observed around the Hamama-Beida transition, which corresponds to the K-Pg transition.

Conversely, the $\delta^{34}S$ values demonstrate an opposing trend compared to the $\delta^{15}N$ values. The strata with the heaviest values are found in the rhythmically laminated mudstone of the Upper Member, reaching up to 3‰. Depleted strata are observed around the transition from the latest Maastrichtian to the earliest Danian (Zones CC26a to NP3; Fig. 10), with a minimum as low as −43.2‰ (Fig. 10). Moving further up-section, $\delta^{34}S$ values indicate a gradual enrichment, reaching values as high as −1.3‰ around the NP3-NP4 zonal transition, which coincides with the peaks in TOC% and HI (Fig. 10).

4.6. Re-Os isotopes

This study shows Re-Os isotope data that extend tens of meters above and below the K-Pg transition, providing a broader perspective. The temporal distributions of $^{187}Os/^{188}Os$ and $^{187}Re/^{188}Os$ ratios both exhibit similar patterns (Fig. 10). The $^{187}Os/^{188}Os$ values are mostly ≥ 1, surpassing the average composition of Cenozoic seawater (0.2–1.06, Ravizza, 2001), with a maximum observed during the lowermost Dakhla TOC spike (~3.7). However, the $^{187}Re/^{188}Os$ ratios are generally lower than for average seawater composition, with a peak occurring in the lowermost Dakhla TOC peak (~2709). A slight depletion in both ratios was observed around the Hamama-Beida transition (K-Pg), reaching values as low as 1.2 and 575 for $^{187}Os/^{188}Os$ and $^{187}Re/^{188}Os$, respectively (Fig. 10). Most samples exhibit $^{187}Os/^{188}Os$ and $^{187}Re/^{188}Os$ ratios higher than the average continental crust (1.05–1.4 and 34.5, respectively; Peucker-Ehrenbrink and Jahn, 2001).

5. Discussion

5.1. Climatic perturbation

The late Cretaceous time was marked by a global cooling trend, which led to a sea-level lowstand at ~ 65.5 Ma (Li and Keller, 1998). In the Quseir section, the Campanian-Maastrichtian period is consistent with the overall global cooling trend (Linnert et al., 2014; Thibault et al., 2016; Linnert et al., 2017). Interestingly, the late Maastrichtian experienced two warming events (Thibault and Husson, 2016) that were attributed to the global impact of the Deccan volcanism (e.g., Courtillot et al., 1986; Ravizza and Peucker-Ehrenbrink, 2003). Chenet et al. (2009) proposed that Phase 2 of the Deccan volcanism (the most intense phase) could have contributed to shaping the widespread and stressful environmental conditions represented in the K-Pg event. These two transient warming episodes are observable in the Quseir section (Fig. 5). The first warming episode, during the *Lithraphidites quadratus* (CC25b) Subzone, coincides with Phase 1 of the Deccan volcanism from 68.36 to 66.99 Ma (Gradstein et al., 2004; Keller et al., 2012). Conversely, the CC26a Subzone in the Quseir region exhibited a cooling trend, as evidenced by higher positive $\delta^{18}O$ readings (e.g., Keller et al., 2002). The warm-water species *W. barnesiae* decreased in number during this cooling episode, while cold-water species such as *A. cymbiformis*, *M. staurophora*, and *B. constans* thrived (Fig. 5). Furthermore, the latest Maastrichtian warming episode is thought to have occurred at a period of stressful conditions, which may be connected to global climate change. This interpretation is based on the occurrence of the *Micula prinsii* Subzone (CC26b), which is associated with Phase 2 of the Deccan volcanism during the latest Maastrichtian (Keller et al., 2002; Keller et al., 2012; Punekar et al., 2014). Additionally, the early Danian zones NP2-NP4 were deposited during an overall warm climate trend, as evidenced by the increased abundance of *C. pelagicus* and *E. subpertusus*, which is consistent with the findings of Keller et al. (2002) and Tantawy (2003).

CIA has been widely utilized to evaluate the degree of chemical weathering. High CIA values are often associated with warm and humid paleoclimatic conditions and depleted CIA values (typically below 60) indicate weak or absent chemical weathering effects corresponding to cooler and/or arid paleoclimate (Nesbitt and Young, 1982; Zhai et al., 2018; Zhang et al., 2021). Moreover, K-metasomatism can influence CIA values, and therefore we used the A-CN-K ternary diagram (Fig. 9) following Fedo et al. (1995). The diagram reveals that the Quseir core section largely conforms to the ideal weathering trend (the violet arrow in Fig. 9), indicating a minimal influence of K-metasomatism. Most samples from the

Quseir section are situated within the moderately and intensively weathered rocks field according to the diagram (Fig. 9). An exception is observed in the Upper Member of the Duwi Formation, which consists of rhythmic and wavy laminated silty mudstone layers located within the slightly to moderately weathered rocks field (Fig. 9).

To ensure reliable paleoclimatic reconstructions using CIA values, it is desirable to consider first-cycle sediments to minimize the reworking effect (Roy and Roser, 2013). Major and trace element contributions in fine-grained clastic rocks can be utilized to determine the source of sedimentary material (McLennan and Taylor, 1991; Garver et al., 1996). Certain metals (Ti, Zr, Th, La, Y, and Sc) are reliable indicators of sedimentary provenance due to their low solubility and high stability during geological processes. Based on cross-plots of TiO_2 vs. Zr (Hayashi et al., 1997; Fig. 11A), Th/Co vs. La/Sc (Cullers, 2002; Fig. 11B), and Cr/V vs. Y/Ni (Hiscott, 1984; Fig. 11C), it can be inferred that most of the studied intervals originated primarily from an intermediate or mixed felsic/mafic igneous protolith with minor felsic affinity. The Th/Sc vs. Zr/Sc cross-plot indicates the potential influence of sediment recycling during deposition (McLennan et al., 1993; Fig. 11D), which aligns with the previously suggested protolith composition. Furthermore, the relatively depleted Zr/Sc ratios in the Quseir section suggest that the compositions were predominantly influenced by the parent rock composition with limited or no contribution from a recycled source, supporting the findings of Fathy et al. (2018). Based on the preceding analysis, the CIA values in the Quseir section exhibit an increasing trend towards younger sediments, with values mostly exceeding 65 (Fig. 8). However, the Upper Member stands out as an exception, displaying lower CIA values as low as 56 (Fig. 8). These values are below the average shale values (70–75; Nesbitt and Young, 1982), and could be attributed to the relatively coarser nature of the sediment and its proximity to the hinterland. Notably, a similar moderate grade of chemical weathering was recorded during the Late Campanian in Egypt's Western Desert (Fathy et al., 2023b).

Refractory elements such as Al and Ti are major components that are not sensitive to variations in redox conditions and to diagenetic processes (Yarincik et al., 2000). Al is typically found in fine-grained aluminosilicates (clays) that are formed through intense chemical weathering under warm/humid climates (Zhang et al., 2021). On the other hand, Ti is predominantly present in the form of heavy minerals, transported into the marine system through wind action, particularly in arid climates (Beckmann et al., 2005). As a result, the Al/Ti ratio is primarily controlled by the protolith and the delivery mechanism under specific climatic conditions, where its variability can be used as a paleoclimate proxy for marine sediments (Yarincik et al., 2000; Zhang et al., 2015; Zhai et al., 2018; Zhang et al., 2021). Elevated values indicate significant fluvial input under a humid climate, while low values suggest a greater contribution from windblown sources in an arid climate. A general correspondence is observed between the profiles of Al/Ti ratios and CIA values in the Quseir section (Fig. 8). This alignment suggests a relatively cooler, windier, and comparatively more arid climate during the late Cretaceous strata of the study section. The Beida Member (Danian) is characterized by a warm/humid climate, which led to intensified chemical weathering and an increased influx of weathered detritus from the hinterland. These findings support the climate-related interpretations derived from the calcareous nannofossils. The persistently warm/humid climate during the deposition of the Dakhla Formation likely led to intensified continental weathering and elevated runoff influx, resulting in the delivery of nutrient-rich sediments to the marine ecosystem. This, in turn, would have facilitated water column stratification and enhanced the preservation of organic matter.

5.2. Paleo-redox evolution

As indicated in Algeo and Tribovillard (2009), it has been observed that low-oxygen marine systems display patterns of Mo-U covariation, which can be linked to distinct characteristics and processes within the depositional environment. These include variations in benthic redox conditions, the functioning of particulate shuttles within the water column, and variations in watermass chemistry. Therefore, it is crucial to explore the Mo-U covariation within the studied strata to gain valuable insights.

The variations in Mo content within the analyzed section approximately parallel the profile of TOC (Fig. 8), being positively correlated with organic carbon. This suggests that Mo is predominantly sequestered through complexation with organic matter, although other mechanisms may also play a role (e.g., Phillips and Xu, 2021). The Mo enrichment factor (Mo_{EF}) within the study section can be categorized as follows: values ranging from 1 to 10 (Lower and Upper members of Duwi Formation; Fig. 8), values oscillating around an enrichment factor of 10 but remaining below 100 (Middle, Uppermost, Hamama, and the majority of Beida members; Fig. 8), and values exceeding 100 (lowermost Hamama Member and the carbonate-rich bed in the Beida Member at depths of $\sim$ 80–100 m; Fig. 8). Mo_{EF} values between 1 and 10 typically indicate non-euxinic conditions characterized by the presence of H_2S in the pore water. Mo_{EF} values exceeding 100 suggest persistently euxinic conditions, indicating the possible coexistence of Mo and H_2S in the water column (Scott and Lyons, 2012). The relatively moderate Mo_{EF} values (10–100) observed in a significant portion of the Quseir section can be attributed to one or more factors. These factors may include (1) a dilution effect resulting from significant detrital input due to a high sedimentation rate, (2) variations in water column pH where Mo precipitation is inversely proportional to pH (Helz et al., 2011), (3) a Mo-depleted euxinic environment, and (4) an intermittently euxinic water column within an environment that fluctuates between euxinic and anoxic non-euxinic conditions (Scott and Lyons, 2012). Among these factors, the third and fourth explanations appear more plausible, as the sedimentation rate ranged 25–35 m/Ma and no substantial evidence of dramatic pH variations was observed.

In oxic environments, Mo is predominantly soluble and exists as the molybdate anion. However, in the presence of free H_2S in the water column or pore water, the molybdate anion can rapidly transform into the thiomolybdate form. This form can be effectively scavenged and incorporated into sediments through processes such as organic matter adsorption and the formation of authigenic minerals, leading to significant Mo enrichment in sediments (Algeo and Lyons, 2006; Tribovillard et al., 2006). On the other hand, U remains in a conservative form under oxic conditions but can be reduced to an insoluble form at the sediment–water interface in anoxic conditions, resulting in its removal and subsequent sequestration in the sediment (Algeo and Lyons, 2006; Tribovillard et al., 2006; Algeo and Tribovillard, 2009). Furthermore, Mo has a higher affinity for binding with oxyhydroxides compared to U. Therefore, the covariation of Mo and U enrichments can be utilized to identify the Fe-Mn shuttling effect, where elevated Mo enrichments occur without a corresponding increase in U enrichments (Algeo and Tribovillard, 2009). Consequently, anoxic-euxinic settings are favorable for the preservation of Mo and U, leading to higher enrichments of them in sediments compared to suboxic-oxic sediments (Tribovillard et al., 2006; Algeo and Rowe, 2012).

The data from the studied Quseir section demonstrates a generally high degree of enrichment for Mo and U, with the proportion of Mo and U mostly being 1–3 times that of seawater for most samples from the Middle, Hamama, and Beida members (Fig. 12A).

However, samples from the Lower, Upper, and a portion of the Uppermost members of the Duwi Formation exhibit proportions of Mo and U ranging 0.3–1 times that of seawater (Fig. 12A; Algeo and Tribovillard, 2009). In this discussion, we examine the intervals of the studied Quseir section in oxygen-deficiency decreasing order, from more anoxic to less oxygen-deficient conditions.

The plot suggests the persistence of more oxygen-depleted conditions during the deposition of the Middle Member and the Dakhla Formation. This is indicated by a higher enrichment of Mo compared to U, with some samples falling outside the unrestricted marine zone, suggesting a certain degree of restriction. The Mn-Fe oxyhydroxides shuttling in a few samples from the Middle Member of the Duwi Formation accelerates the transfer of Mo to the seafloor, resulting in a strong enrichment of authigenic Mo over U (Algeo and Tribovillard, 2009). Furthermore, a significant portion of samples from the Lower and Uppermost members predominantly fell within the range of 0.3–1 times the marine water proportion. However, some samples from the Uppermost Member exhibit proportions lower than 0.3, indicating a higher enrichment of U without a corresponding enrichment in Mo (Fig. 12A). This can be attributed to the association of phosphorite strata in this Member, suggesting possibly suboxic to intermittently anoxic conditions. Lastly, the Upper Member demonstrates very limited enrichment of both Mo and U, primarily falling within the oxic zone of the diagram (Fig. 12A).

5.3. Hydrographic restriction assessment

The availability of seawater Mo is governed by hydrographic restriction (Algeo and Lyons, 2006). The Mo/TOC ratio is commonly used to assess the degree of sub-chemoclinal watermass restriction during sedimentary rock deposition (Fig. 12B-C; Algeo and Lyons, 2006). Unrestricted oxygen-deprived conditions result in high Mo/TOC ratios due to enhanced watermass exchange ($\sim$45 ± 5 μg g^{-1}/%), while Mo/TOC ratios tend to decrease with increasing watermass restriction (as low as $\sim$4.5 ± 1 μg g^{-1}/%; Algeo and Lyons, 2006). The lower Mo/TOC ratio can be plausibly explained by Mo depletion in seawater during sediment accumulation, attributed to limited deep-water renewal known as the basin reservoir effect (Algeo and Lyons, 2006; Chang et al., 2018). Additionally, the decreased aqueous Mo concentration may be a result of Mo removal to sediments in weakly euxinic environments with insufficient re-supply through deep-water renewal (Algeo and Lyons, 2006).

Indeed, basin restriction has been documented on the Egyptian shelf during the late Cretaceous deposition, with several paleo-high areas reported in northern Egypt (Said, 1990; Barrier and Vrielynck, 2008), which were tectonically active during earlier periods (Bevan and Moustafa, 2012). Basin restriction has also been observed during the Paleogene period, where the deposition was likely triggered by a significant tectonic event resulting from the folding and/or inversion of the Syrian Arc (Höntzsch et al., 2011), leading to differential uplifts and subsidence during phases of extension and intervening inversion events (e.g., Bosworth and Tari, 2021). The circulation in the paleo-lows would have been partially restricted, causing the base of the water column to become bathymetrically isolated and oxygen-deprived across the shelf (Robinson, 1995). Additionally, well data has shown the disappearance of the Campanian Brown Limestone source rock Formation in the north of the southern edge of the inversion structure. This suggests that these structures provided a paleo-topographic relief, influencing the distribution of the organic-rich facies (Bevan and Moustafa, 2012).

The Algeo and Lyons (2006) model is most effective for samples deposited under anoxic conditions. Therefore, for the Mo-TOC covariation, samples with Mo_{EF} values > 10 were selected from each Member (Fig. 8 & 12B-C). The cross-plot suggests that a significant portion of the samples fell within either the Black Sea or the Framvaren Fjord trend (Upper, Hamama, and Beida members), while only two samples from the organic-rich TOC peak of the Hamama Member plot within the Cariaco Basin trend (Fig. 8 and 12B-C). This indicates an overall depletion of seawater Mo concentration in at least semi-restricted sub-chemoclinal conditions (Algeo and Lyons, 2006). Furthermore, the Mo/TOC profile (Fig. 8) reveals that the majority of samples plot in the strongly restricted field, excluding the lowest Dakhla TOC peak. Specifically, the Middle, Uppermost, Hamama, and Beida members have average Mo/TOC ratios of 4.9, 6.0, 3.4, and 3.2 μg g^{-1}/%, respectively. When compared to the average value of euxinic sediments from the latest Proterozoic-Phanerozoic (27 μg g^{-1}/%; Scott et al., 2008), these data suggest an overall depletion of the seawater Mo reservoir under a certain degree of sub-chemoclinal watermass restriction (Algeo and Lyons, 2006).

From another perspective, strong element enrichments may have occurred due to local factors, such as stratigraphic condensation resulting from significantly low sedimentation rates, rather than global oceanic changes (Miller et al., 2017). Therefore, the sedimentation rate factor plays an important role in Mo sequestration within a basin. For instance, the highest abundances of TOC and Mo are found in the lowermost Hamama Member, as these strata are considered a maximum flooding surface systems tract (El-Shafeiy et al., 2016). The substantially reduced sedimentation rate might have hindered the dilution of organic carbon and Mo contents and/or supplied Mo renewal to the system via transgression. These conditions persisted under oxygen-deficient seawater until the sedimentation rate increased again during the deposition of the rest of the Hamama strata and the overlying Beida Member (Fig. 8).

5.4. Productivity

Eshet et al. (1992) and Eshet and Almogi-Labin (1996) conducted productivity estimations by analyzing the abundance of calcareous nannofossil species and comparing their distribution with that of other organisms, such as planktonic foraminifera (Almogi-Labin et al., 1993) and organic-walled dinoflagellate cysts (Eshet et al., 1994). Their findings revealed that relative species abundances were influenced during periods of high productivity, while calcareous nannofossil diversity and abundance reached optimal conditions during periods of low productivity. During high productivity periods, an adverse effect was observed by Thunell and Sautter (1992), where the planktonic foraminiferal occurrences increased at the time of diminishing the calcareous nannofossil population. In contrast, Young (1994) hypothesized that calcareous nannofossil abundance increased with high productivity but declined in hyper-eutrophic settings. The Quseir section offers additional insights into the relationship between calcareous nannofossil abundance, species diversity, and environmental conditions in this region of central Egypt. Notably, Tantawy (2003) confirmed the relationship between calcareous nannofossils and productivity that observed in other regions of the Tethys. He observed that during the late Maastrichtian, high abundance and species richness of calcareous nannofossils were associated with low surface productivity. There is a notable increase in low-productivity taxa during the late Cretaceous in the Quseir section, with only sporadic occurrences of high-productivity taxa. Meanwhile, calcareous nannofossils exhibit high species richness values, which aligns with the findings of Keller et al. (2002). The decline in productivity towards the end of the Maastrichtian is consistent with similar trends observed in other regions of the Tethyan Ocean (e.g., Barrera and Keller, 1994; Keller et al., 2002; Keller et al.,

2012). The observed patterns in calcareous nannofossil species richness are similar to those reported by Keller et al. (2002), except for the CC25b Subzone, where both abundance and species richness were lower. This decline could be attributed to poor preservation and/or the presence of a shallow, stressed environment in the Quseir region. During the Danian period, productivity was high, as indicated by the sporadic occurrence of high-productivity taxa within the NP3 and NP4 zones. This finding is consistent with the conclusions of Tantawy (2003), where high surface productivity was inferred from the $\delta^{13}C$ signature of bulk sediments.

Although TOC content usually represents a small fraction of the total primary productivity in an aqueous system, it serves as a primary proxy for productivity, depositional environment, and preservation (Canfield, 1994). Moreover, HI data are valuable for distinguishing the sources of sedimentary organic matter. The temporal distribution of TOC and HI (Fig. 10) approximately corresponds to the denudation of calcareous nannofossils distribution (Fig. 5). On average, the Duwi Formation exhibits lower values of TOC and HI compared to the Dakhla Formation. The discrepancy between the temporal distribution of TOC and HI contents and that of the productivity-related calcareous nannofossils taxa can be attributed to the presence of other phytoplankton and their ability to perform photosynthesis during the K-Pg time (e.g., Sepúlveda et al., 2019).

5.5. Implications from $\delta^{13}C_{Org}$ – $\delta^{15}N$ patterns

The carbon and nitrogen isotopic signature can provide valuable information on organic productivity and C-N cycling. Bulk $\delta^{13}C_{Org}$ can, on average, indicate the carbon isotope composition of the preserved organic carbon in sediments (Meyers, 1997; Hayes et al., 1999). It is worth mentioning that the studied strata in the Quseir section contain organic matter that is either immature or very early mature ($T_{max} \leq 440$ °C; El-Shafeiy et al., 2017). Therefore, the $\delta^{13}C_{Org}$ values were not influenced by thermal degradation during maturation processes, which commonly result in the loss of light carbon isotopes with generated hydrocarbon, leaving behind residual organic carbon enriched with the ^{13}C isotope. Thus, the data presented here largely represent the primary signature. The variability in $\delta^{15}N$ values in the Quseir section can be mostly attributed to changes in denitrification in the water column, nitrogen fixation, and/or nutrient uptake by phytoplankton when nitrate was sufficient (Robinson et al., 2012).

Most Cretaceous organic-rich strata consist of marine organic matter with depleted $\delta^{13}C_{Org}$ values between −28‰ and −26‰ (Dean et al., 1986) due to the availability of dissolved CO_2 during the high pCO_2 conditions of the Cretaceous period. Furthermore, the generally depleted $\delta^{13}C_{Org}$ in the late Maastrichtian and early Danian strata can be attributed to the contribution of light atmospheric carbon linked to the released CO_2 from the Deccan volcanism (Rosenberg et al., 2021). Examining the $\delta^{13}C_{Org}$ of the Quseir section reveals temporal heterogeneity in the bulk $\delta^{13}C_{Org}$ archives (Fig. 10). A slight negative carbon isotopic shift, reaching a minimum of −29‰, is observed in the Middle Member of the Duwi Formation, where predominantly mixed marine organic matter was preserved (kerogen type II; Fig. 10). A plausible explanation for this observation is the surface water stratification during the deposition of these strata (El-Shafeiy et al., 2014; 2017). The stratified water column caused the isotopically light organic matter that underwent oxidation to be retained at the bottom of the photic zone, leading to a shift towards lighter isotopic values in photosynthesizers. A similar explanation was proposed for the mid-Cretaceous black shales in the Kerguelen Plateau (Meyers et al., 2009).

The $\delta^{13}C_{Org}$ values of the Upper Member, however, are relatively heavy, reaching a maximum of −24.5‰, compared to the rest of the Quseir section (Fig. 10). This observation suggests an increased input of detrital plant debris and terrestrial organic matter (e.g., Kodina, 2002) to the proximal side of the shelf, which was preserved in this Member. In contrast, the $\delta^{15}N$ values of this Member exhibit the lightest values along the Quseir section, approaching the $\delta^{15}N$ value of C3 land plants (+0.5‰; Peterson and Howarth, 1987; Fig. 13). Therefore, the light $\delta^{15}N$ values also indicate that the organic material is mainly derived from terrestrial plants, predominantly C3 plants with a $\delta^{13}C_{Org}$ value of approximately −27‰ (Meyers, 1997). This is also confirmed by its HI values (Fig. 10). Oxygenated conditions have seemingly prevailed during this member, where the $\delta^{15}N$ signature shifts to lighter values compared to the Middle Member. However, the $\delta^{15}N$ values remained heavier than those typically observed in C3 plants. This discrepancy could be attributed to the re-mineralization process and the release of isotopically light NH_4 (e.g., Prahl et al., 2003) that have altered the $\delta^{13}C_{Org}$ signature, resulting in heavier values after the release of ^{13}C-depleted carbon back into the (in)organic carbon pool (e.g., Freeman, 2001). Similarly, the relatively organic-lean strata of the NP2 Zone are also characterized by organic material of terrestrial origin (Fig. 10), where the $\delta^{13}C_{Org}$ values approximate those of present-day C3 land plants (~-27‰; Fig. 8; Meyers, 1994).

Shifts of a magnitude ~ 2‰ to lower values are noticeable in both $\delta^{13}C_{Org}$ and $\delta^{15}N$ at the lowermost and organic-richest layer in the Hamama Member across the CC25b-CC26a transition, right above the warm Episode 1 (Figs. 5 and 10). This layer represents a maximum flooding surface systems tract (El-Shafeiy et al., 2016) and contains typical marine organic material (Fig. 10). Hence, a higher quantity of land plants is a rather unlikely explanation for such isotope depletions. Instead, this layer shows the peak of high-productivity taxa (Fig. 5). The isotope data of $\delta^{13}C_{Org}$ and $\delta^{15}N$ were seemingly influenced by local factors (such as stratigraphic condensation) that affected the isotopic fractionation during nitrogen and carbon fixation by primary producers. As this layer demonstrates high productivity and an oxygen-deficient water column, it can be suggested that an elevated denitrification rate would have led to an environment with limited inorganic dissolved nitrate, and thereafter motivating nitrogen fixation occurred possibly aided by bacteria, and thus diluting the isotopic signature via isotopically light N_2 input (e.g., Cao et al., 2021). However, it is unlikely to explain the $\delta^{15}N$ excursion as a testimony to nitrogen fixation by diazotrophs, which yields lower $\delta^{15}N$ values from −3‰ to + 1‰ (Kuypers et al., 2004; Ader et al., 2016). Like nitrogen, the carbon isotope signature seemingly resulted from an episodic recycling of isotopically-light CO_2, which influenced the ^{13}C content of the bio-produced organic material. This model was postulated in the Toarcian oceanic anoxic event in the presence of photic zone euxinia (Küspert, 1982; Schouten et al., 2000). The degradation of organic matter by anaerobic bacteria under an oxygen-deficient water column can produce isotopically-light CO_2 that can accumulate underneath the redox boundary and can be combined with surface waters (Schouten et al., 2000). Another possible factor can also be the diagenetic consequence, where differential removal of ^{13}C-enriched and ^{15}N-enriched fractions (e.g., carbohydrates and proteins) took place and led to a negative shift in $\delta^{13}C_{Org}$ and $\delta^{15}N$ compared to the bulk algal matter (Meyers, 1994; Lehman et al., 2002). It is worth mentioning that light $\delta^{13}C_{Org}$ (-29‰) and $\delta^{15}N$ (-4.5 to −5‰) values were recorded at the onset of the Oil Shale Member of the Negev section representing a maximum flooding surface systems tract with a TOC peak up to ~ 20% (Meilijson et al., 2018). The isotope shift was attributed to the early mineralization of organics during the denitrification process and the preferential breakdown of the protein component in oxygen-deficient bottom-water conditions (Schneider-Mor et al., 2012). Bacterial ingrowth can supply $\delta^{15}N$-depleted components to the organic material that boosts the lower

$\delta^{15}N$ values (Libes and Deuser, 1988). However, the influence of selective diagenesis of isotopically heavy or light organic fractions is usually small (<2‰; Dean et al., 1986; Meyers, 1997).

The TOC and HI peaks in the CC26-NP2 zones coincide with an increment in the $\delta^{15}N$ values (Fig. 10), which implies increased denitrification rates resulted from productivity-induced expansion of oxygen-deprived conditions (Cao et al., 2021). The enrichment in $\delta^{15}N$ around the K-Pg transition in the Quseir section, reaching a maximum of + 8.6‰, can be attributed to increased bacterial denitrification and/or phytoplanktonic nitrate assimilation due to increased marine productivity (high TOC and Type I kerogen; Fig. 10). Similar trends were observed in El Kef and Aïn Settara sections (Sepúlveda et al., 2019). Alternatively, the $\delta^{13}C_{Org}$ shows a negative shift of magnitude −2.8‰ close to the K-Pg transition that appears to be of a global pattern that has a magnitude between −0.5 and −3.0‰ (Meyers, 1992), being observed in several sections including El Kef and Aïn Settara sections (Sepúlveda et al., 2019). This excursion was believed to signify a depressed productivity period during the early Danian where organic matter could have re-mineralized quicker than being biosynthesized (Meyers, 1992; Esmeray-Senlet et al., 2015). However, this interpretation is seemingly not the only factor, as relatively elevated TOC and HI values are observable right above the K-Pg transition (Fig. 10). Another important influence could be the intensified volcanic CO_2 in the atmosphere resulting from the Deccan phase 2 eruption that may have resulted in negative $\delta^{13}C$ excursion around the K-Pg transition (Sial et al., 2016; Fig. 10).

The cross-plot of $\delta^{15}N$ vs. $\delta^{13}C_{Org}$ provides valuable insights into the origin of organic matter (Fig. 13). Comparing our data with the data from Meyers (1997) can imply that our section encompasses $\delta^{13}C_{Org}$ values that mimic, on average, the Cenomanian-Turonian (C/T) black shale values except for the Upper Member that contains heavier values (Fig. 13). However, the $\delta^{15}N$ data diverge significantly from the C/T black shales, instead resembling the $\delta^{15}N$ values observed in marine plankton (+8.6‰) and dissolved nitrate (+7‰ to +10‰) for most intervals (Fig. 13; Meyers, 1997). Additionally, our $\delta^{15}N$ data partly resembles those of El Kef and Aïn Settara sections in Tunisia (Fig. 13; Sepúlveda et al., 2019). Notably, the Upper Member shows $\delta^{15}N$ values similar to those of the California River and the Black Sea (Fig. 13). The diagenesis of the organic matter via microbial effect in most intervals of the Quseir section has caused a slight deviation from the typical $\delta^{15}N$ values. The denitrification of the nitrate anion in anoxic water conditions selectively releases light nitrogen isotopes, leaving the remaining nitrate enriched in the heavy isotope that is available for algal utilization (Meyers et al., 1997). Instead, Schneider-Mor et al. (2012) implied that the main mechanism that determines the $\delta^{15}N$ values in the Negev section, which is deeper marine than the Quseir section, was the selective decomposition of specific organic fractions via denitrification and/or anammox. They recorded an increasing trend in the $\delta^{15}N$ values from the base of the section (top Phosphate Member) to the Marl Member, which can mirror a decline in the preferential removal of N-rich components with changing from anoxic to more oxygenated benthic conditions (Fig. 13). Our data from the Quseir section, however, demonstrates overall higher $\delta^{15}N$ values than those from the Negev section (Fig. 13). We assume that this discrepancy is due to the less efficient selective decomposition process in the Quseir section, possibly influenced by its proximity to land and the non-persistent anoxic/euxinic conditions. These findings align with the presence of Type III kerogen and less anoxic intervals in the Quseir section.

5.6. Implications from pyrite $\delta^{34}S$ profile

The sulfur isotope composition of sulfides preserved in sedimentary records can potentially reflect that of sulfides formed during sulfate reduction processes but with greater depletion (Canfield, 2001). Assimilatory sulfate reduction occurs in autotrophic organisms and results in minimal isotopic fractionation, whereas dissimilatory sulfate reduction is typically carried out by heterotrophic organisms (bacterial sulfate reduction) under reducing conditions (Sharp, 2017). Dissimilatory reduction plays a key role in the sulfur budget evolution within an ecosystem, having a rate that is inversely proportional to the magnitude of fractionation (ranging 3–46‰, averaging 18‰; Canfield et al., 1998; Canfield, 2001; Sharp, 2017). During sulfate reduction, H_2S is typically ^{34}S-depleted, and subsequent pyrite formation occurs. Moreover, the disproportionation processes of sulfur intermediate compounds generate significant fractionation, which can explain the highly depleted sulfides $\delta^{34}S$ values observed within marine sediments (Canfield and Thamdrup, 1994; Canfield and Teske, 1996 Canfield et al., 1998; Böttcher and Lepland, 2000). Disproportionating bacteria are found in high abundance in sediments at the sediment–water interface, where bioturbation may occur (Böttcher et al., 2001). However, it has been reported that marine sulfate-reducing bacteria can deplete ^{34}S by up to 66‰ relative to sulfate through reduction solely, without involving oxidative sulfur cycling (Sim et al., 2011).

It is noteworthy that the study strata exhibit four distinct morphologies of disseminated syn- and diagenetic pyrite, as observed by Soliman and El Goresy (2012). These morphologies include grouped multi-framboids, individual framboids, growth idiomorphic framboids, as well as single and aggregated euhedral pyrite crystals. Among these, the two predominant types are the multi-framboids and individual framboids. Soliman and El Goresy (2012) reported that around 75% of individual framboids have an average size ranging between < 5 μm and 5–10 μm.

Strong variations were observed in the pyrite $\delta^{34}S$ profile in the Quseir section (Fig. 10) due to the heterogeneous nature of sulfate reduction and pyrite formation processes (McKay and Longstaffe, 2003). In particular, the Duwi Formation exhibits a higher and abrupt temporal variability in $\delta^{34}S$ values (-31.4 to + 28.1‰) compared to the overlying Dakhla Formation (-42.1 to + 2.4‰). The Upper Member is signified by its highly positive $\delta^{34}S$ values, averaging + 13.1‰ (Fig. 10), which are indicative of surface runoff sulfur precipitation (+3 to + 15‰; Chen et al., 2020). It is important to note that the $\delta^{34}S$ values of sulfide can serve as a sedimentary record not only for the origin of sulfur but also for the concentration of sulfate in the water (Canfield, 2001). Considering that the Upper Member was identified as a lowstand systems tract with relatively more oxygenated conditions, a significant amount of runoff water and coarser sediments were transported to the shelf system. The limited extent of sulfate reduction can be confirmed by the significantly decreasing pyrite and Mo contributions throughout this interval (Figs. 8, 10, and 12A). Consistently, high pyrite $\delta^{34}S$ values were observed in the Duwi phosphorites (Baioumy, 2011), as well as in the late Cretaceous hydraulically-connected coastal plain silts and sands of the Marshybank Formation (+13.2‰; McKay and Longstaffe, 2003). The latter study explained the ^{34}S enrichment as a result of dissolved residual sulfide, enriched in ^{34}S, migrating from overlying marine sediments, which was also observed in brackish and freshwater sediments. Another important factor is the re-oxidation of sulfide, where ^{32}S-sulfide was likely consumed at a faster rate than ^{34}S-sulfide (Fry et al., 1988), leading to an increase in the $\delta^{34}S$ values of the remaining sulfides.

During the two Mo-rich spikes that represent the lowermost stratum of the Hamama Member (at ~ 230 m) and carbonate-rich strata (at 80–90 m depth; Fig. 10), the presence of anoxic-sulfidic bottom waters likely indicates significant sulfide formation through high rates of sulfate reduction. This process led to a depletion of sulfate and an enrichment of remaining porewater sulfate in ^{34}S, resulting in pyrites with slightly depleted $\delta^{34}S$ values com-

Table 2
Re and Os analysis data and their isotope data for samples from the Quseir section. Initial $^{187}Os/^{188}Os$ ratios were computed based on 65 Ma.

Sample	Re (ppb)	2RSE(%)	Os (ppb)	2RSE	$^{187}Re/^{188}Os$	2 s%	$^{187}Os/^{188}Os$	2 s	Rho	$^{187}Os/^{188}Os_i$
171.70	74.8	0.02	0.565	0.21	714	0.24	1.178	0.003	0.93	0.40
187.50	48.4	0.02	0.456	0.26	575	0.30	1.217	0.003	0.96	0.59
191.80	66.8	0.02	0.586	0.25	614	0.26	1.170	0.009	0.23	0.50
203.60	80.3	0.02	0.505	0.24	897	0.28	1.578	0.004	0.94	0.61
211.40	38.7	0.02	0.445	0.27	464	0.30	1.076	0.003	0.94	0.57
218.50	46.9	0.02	0.536	0.22	470	0.25	1.131	0.002	0.97	0.62
225.20	56.8	0.04	0.619	0.19	477	0.21	0.860	0.002	0.91	0.34
228.30	330	0.03	0.84	0.35	2689	0.50	3.552	0.017	0.98	0.64
230.30	328	0.02	0.84	0.35	2709	0.51	3.679	0.018	0.99	0.74
233.00	5.72	0.06	0.122	0.96	244	1.05	0.905	0.008	0.97	0.64
240.60	14.9	0.02	0.129	0.90	639	1.0	1.413	0.013	0.99	0.72
245.10	58.4	0.03	0.668	0.22	471	0.24	1.171	0.002	0.74	0.66

pared to other intervals (Canfield, 2001; Pasquier et al., 2021; Fig. 10). This interpretation is supported by the elevated pyrite content observed in these specific intervals (Figs. 8 and 10).

Immediately above the TOC peak in the lowermost Hamama Member, and up to a depth of 140 m, including the K-Pg transition, there are significantly depleted pyrite $\delta^{34}S$ values, reaching a minimum of −43.8‰ at 150 m depth (Fig. 10). From the CC26b Zone to the K-Pg transition, which encompasses substantially higher pyrite contents (Fig. 10), neither TOC% nor HI values indicate oxic conditions. Low marine sulfide $\delta^{34}S$ values can indicate bacterial sulfate reduction and pyrite formation in a sulfate-replete (or open) pore system (McKay and Longstaffe, 2003). Comparably, low $\delta^{34}S$ values of sulfides have been reported in the dissolved sulfide just below the oxic-anoxic boundary of the water column in the Black Sea and the Cariaco Trench (−36 to −38‰; Fry et al., 1991). However, some samples from this interval show significantly lower values. Therefore, diagenetic processes can explain low pyrite $\delta^{34}S$ values in this interval by causing disproportionation of sulfur intermediates in organic-lean strata or by sulfate reduction without extracellular oxidative sulfur cycling (Sim et al., 2011). However, from the K-Pg transition to 140 m depth, there is a gradual decline in pyrite content, as well as TOC%, HI, and Mo contributions, being minimum during the NP2-NP3 transition (Figs. 8 and 10). This suggests a gradual decrease in the rate of sulfate reduction, which typically leads to more depleted pyrite $\delta^{34}S$ values. It is possible that disproportionation of sulfur intermediate species occurred, resulting in significantly depleted pyrite $\delta^{34}S$ values.

5.7. Re-Os isotope signature: Seawater vs. Terrestrial

Ancient organic-rich marine sediments can reveal temporal variations in the Os isotope composition of seawater (Cohen, 2004). The present-day seawater $^{187}Os/^{188}Os$ ratio is relatively uniform with a value of 1.06 (e.g., Peucker-Ehrenbrink and Ravizza, 2002), which has significantly changed over time. The major sources of Os isotopes in seawater can include unradiogenic contributions from hydrothermal alterations of juvenile oceanic crust ($^{187}Os/^{188}Os$: ~0.12; Peucker-Ehrenbrink and Ravizza, 2002), unradiogenic contributions from extraterrestrial meteorites and cosmic dust ($^{187}Os/^{188}Os$: ~0.127; Peucker-Ehrenbrin and Ravizza, 1996), or radiogenic contributions from weathering of the continental crust ($^{187}Os/^{188}Os$: ~1.9; Cohen, 2004) via river systems ($^{187}Os/^{188}Os$: ~1.4) and/or aeolian dust ($^{187}Os/^{188}Os$: ~1.05; Peucker-Ehrenbrink and Ravizza, 2002). Compared to the Sr isotope proxy, the Os isotope profiling approach in marine sediments can quickly respond to abrupt changes in input composition or weathering flux to seawater due to the relatively short residence time of Os in seawater (10–40 Ka; Peucker-Ehrenbrink and Ravizza, 2002; Cohen, 2004).

The Re and Os contents of the Quseir section (Fig. 10 and Table 2) are significantly higher than the average upper continental crust (0.03 and 0.198 ppb, respectively; Peucker-Ehrenbrink and Jahn, 2001). These findings support Peucker-Ehrenbrink and Blum's (1998) conclusion that the release of Os from weathered organic-rich shale is equivalent to the release from a much greater volume of upper crustal granites. Additionally, all the $^{187}Re/^{188}Os$ values of the analyzed samples are higher than those of the upper continental crust (34.5; Peucker-Ehrenbrink and Jahn, 2001). However, they are lower than the average composition of present-day seawater (Fig. 10). Similarly, a significant portion of these ratios fell below the typical values for organic-rich sediments (~800; Peucker-Ehrenbrink and Ravizza, 2002). Conversely, most of the $^{187}Os/^{188}Os$ ratios of the examined samples are relatively similar to the average ratio in the upper continental crust (1.4 ± 0.3; Peucker-Ehrenbrink and Jahn, 2001), with an exception observed in the lowermost layer of the Hamama Member (Fig. 10). Whereas these ratios are higher than the present-day seawater composition, they are generally lower than the average organic-rich sediments (2.22 and 2.27; Dubin and Peucker-Ehrenbrink, 2015), except for the lowermost Hamama samples.

Quseir samples exhibit significantly more radiogenic present-day and initial $^{187}Os/^{188}Os$ values (Table 2) than previously studied K-Pg pelagic sections elsewhere (e.g., Ravizza and Peucker-Ehrenbrink, 2003; Ravizza and VonderHaar, 2012, among others). Furthermore, samples from the Duwi Formation contain Re-Os contents, as well as $^{187}Re/^{188}Os$ and $^{187}Os/^{188}Os$ ratios, that are as radiogenic as those reported in samples from the Red Sea phosphate mines (Baioumy et al., 2011). This suggests that the Quseir organic-rich sediments are primarily influenced by increased continental weathering under a warm/humid climate and subsequent influx of $^{187}Os/^{188}Os$ through runoff, likely due to increased exposure resulting from crustal uplifts (e.g., Yin et al., 2023). Such terrestrial influx could have potentially altered the Re and Os geochemistry of the studied sediments, indicating that the initial $^{187}Os/^{188}Os$ values may not reflect the typical marine signature during deposition (Table 2). A weak to moderate correlation (r^2 of 0.38) was observed between Os and TOC%. This suggests that Re/Os isochrons can yield significant uncertainties due to Os drawdown caused by restriction, and the dating method assumes that a group of samples should have a uniform $^{187}Os/^{188}Os_i$ ratio (McArthur et al., 2008). Additionally, organic-rich sediments generally contribute disproportionately to a significant portion of Re (>50 %) and a smaller fraction of Os (5–10 %) inventories in the upper continental crust (Dubin and Peucker-Ehrenbrink, 2015). The recycling of such sediments can contribute to an increased and more radiogenic $^{187}Os/^{188}Os$ values of seawater. Furthermore, $^{187}Os/^{188}Os$ values from restricted basins and coastal areas may differ from those of open ocean seawater due to the influence of local riverine Os input (cf., Yin et al., 2023).

It was suggested that the coeval shift towards more negative $\delta^{13}C$ values and more radiogenic $^{187}Os/^{188}Os$ values during the

Cenozoic era is consistent with the increased weathering on organic- or sulfide-rich rocks on the continent (e.g., Dubin and Peucker-Ehrenbrink, 2015; Yin et al., 2023), which biases the isotope composition towards radiogenic $^{187}Os/^{188}Os$ and depleted $\delta^{13}C$ in marine records (Ravizza and Esser, 1993; Peucker-Ehrenbrink and Ravizza, 2002). However, this explanation should be supported by evidence of older rock exposure as a potential source of radiogenic Os. During the Alpine Cycle, a late Santonian compressional phase affected the African-Arabian plate, leading to widespread E–W to ENE–WSW folds in central Africa, eastern Africa, and the southern Red Sea region (Guiraud et al., 2005; Fig. 1). This compressional phase persisted until the end of Cretaceous. The highly exposed continental provinces in these areas experienced tropical weathering (Guiraud et al., 2005) that may have served as a potential source influencing the Re-Os geochemistry of the Quseir section.

The geochemistry of the studied Quseir section reveals an observable perturbation between the present-day and initial ratios of $^{187}Os/^{188}Os$ and $^{187}Re/^{188}Os$ during the spike in TOC% in the lowermost Hamama Member (Fig. 10 and Table 2). Samples at approximately ~ 230 and 228 m depth exhibit a significant positive shift in these ratios compared to the underlying and overlying strata (Fig. 10), accompanied by notably high Os and Re contents, and negative $\delta^{13}C_{Org}$ shift (section 5.5.; Fig. 10). A similar observation was documented in the *falciferum* Zone of the Toarcian mudstone in Yorkshire (Cohen et al., 2004). It was attributed to an increased rate of oxidative weathering of the continental crust during that time, caused by elevated temperatures resulting from heightened levels of atmospheric CO_2. However, McArthur et al. (2008) reinterpreted the same excursion in Yorkshire as an elevated initial $^{187}Os/^{188}Os$, indicating an increased influx of riverine input that was amplified by marine isolation and subsequent Os drawdown into sediments. This latter interpretation aligns with the condensation and watermass restriction observed in such strata in the Quseir section. Another excursion to higher $^{187}Os/^{188}Os$ ratios was recorded during the late Paleocene thermal maximum in the North Atlantic and Indian Oceans, which is consistent with a global increase in weathering rates (Ravizza et al., 2001). Within the interpretative framework mentioned above, the present study $^{187}Os/^{188}Os$ positive excursion coincides with the observed spike in warm taxa near the same layer (Fig. 5), linked to phase 1 of the Deccan CO_2, representing a transient warming event. Additionally, a step-wise shift from moderately weathered to highly weathered CIA values can be observed for the same layer (Fig. 8). However, the assumption of increased riverine influx may be questioned due to the presence of kerogen Type I organics in this layer. The model proposed by McArthur et al. (2008) investigated the effect on isotopic composition through dilution with freshwater. The model suggests that minor contributions of freshwater could lead to varying initial $^{187}Os/^{188}Os$ ratios. We propose that the local drawdown of Os, resulting from provisional watermass restriction, stratigraphic condensation, and anoxia, is likely linked to runoff inputs during deposition. However, without data from a time-equivalent transect of sections, it remains poorly understood whether the observed shift indicates a regional or global change in seawater isotopic signature during the late Maastrichtian.

6. Conclusions

Based on integrated elemental and isotopic distributions from a biostratigraphically-constrained core in the Quseir area near the northern Red Sea coast, the key conclusions regarding paleoclimatic and paleoenvironmental variations during the K-Pg transition are as follows:

1. Late Cretaceous strata exhibit a global cooling trend with a drier climate and reduced chemical weathering, supported by CIA, Al/Ti ratios, and nannofossil assemblages. Two notable warming episodes coincide with the early phases of the Deccan volcanism. Conversely, early Paleocene deposition indicates a period of warmer/humid climate, evidenced by an increased abundance of warm-water taxa and intensive chemical weathering.
2. Redox-sensitive elements (Mo and U) show enrichments 1–3 times higher than seawater in the Middle, Hamama, and Beida members. Lower, Upper, and Uppermost members display lower redox-sensitive element input due to relatively more oxygenic conditions. Strata deposited under oxygen-deficient conditions suggest a potential association with watermass restriction, as indicated by Mo-TOC covariations.
3. Sporadic occurrences of high-productivity taxa during the Danian period suggest increased productivity compared to the late Cretaceous, consistent with temporal distributions of organic carbon (TOC) and hydrogen index (HI).
4. Examination of sediment core $\delta^{13}C_{Org}$ and $\delta^{15}N$ data reveals vertical heterogeneity influenced by various factors. These include the type and re-mineralization potential of organic matter (Upper Member), redox conditions/preservation efficiency (Middle, Hamama, and Beida members), and stratigraphic condensation and recycling of isotopically light CO_2 (Küspert model) in the lowermost Dakhla TOC peak. While some factors have localized effects, certain isotopic shifts correlate with regional or global sections, such as the negative $\delta^{13}C_{Org}$ shift around the K-Pg transition.
5. Strong variations in pyrite $\delta^{34}S$ are likely due to heterogeneous sulfate reduction and pyrite formation in Quseir sediments. Fluctuations in $\delta^{34}S$ are primarily linked to changes in riverine influx and pore-water openness (Upper Member). Moreover, changes in sulfate reduction rate and redox conditions are associated with spikes in TOC and Mo intervals. Furthermore, diagenetic disproportionation of sulfur intermediate species is influential in the CC26 to lower NP3 zones.
6. The Quseir section exhibits significantly more radiogenic $^{187}Os/^{188}Os$ values compared to pelagic K-Pg sections elsewhere. This difference is attributed to continental weathering products, proximity to land, and runoff influx of $^{187}Os/^{188}Os$ under a greenhouse climate. Therefore, the $^{187}Os/^{188}Os$ ratios may not reflect a typical marine signature. At the onset of the Hamama Member TOC spike, a positive shift in $^{187}Os/^{188}Os_i$ to 0.74 (present-day $^{187}Os/^{188}Os$ of 3.68) occurred. However, without supporting data from a time-equivalent transect, it remains uncertain whether this more radiogenic shift represents a global or regional seawater isotopic change.

CRediT authorship contribution statement

Moataz El-Shafeiy: Conceptualization, Investigation, Visualization. **Daizhao Chen:** Funding acquisition, Investigation. **Zhuyin Chu:** Methodology, Validation. **Mu Liu:** Validation. **Ramadan M. El-Kahawy:** Investigation, Visualization.

Declaration of competing interest

The authors declare that they have no known competing financial interests or personal relationships that could have appeared to influence the work reported in this paper.

Acknowledgement

The authors would like to thank DanaGas Egypt© for permitting the sample collection and providing the geochemical elemental analysis data. The Information Centre of the Egyptian Ministry of Petroleum is thanked for facilitating the sampling issue. The late Professor Ahmed El-Kammar and the Emeritus Professor Ahmed El-Barkooky are thanked for providing technical advice and other logistic issues. We are grateful to the Chinese Academy of Sciences (CAS) for the postdoctoral fellowship for the first author (PIFICAS, 2019PC0014). This work was supported by the National Natural Science Foundation of China (91755210). Many thanks to Prof. Roger Flower, Department of Geography, UCL–University College London, for revising the English of the text and providing some technical advice. We are grateful to the associate editor R. Damian Nance, the editor-in-chief M. Santosh, and three anonymous reviewers for the valuable reviews and the help in improving the manuscript.

Appendix A. Supplementary material

Supplementary data to this article can be found online at https://doi.org/10.1016/j.gr.2023.12.007.

References

Abdel Razik, T., 1972. Comparative studies on the Upper Cretaceous-Early Paleogene sediments on the Red Sea Coast, Nile Valley and Western Desert, Egypt. 9th Arab Petrol. Cong. Algiers 3B, 71–123.

Abed, A.M., 2013. The eastern Mediterranean phosphorite giants: An interplay between tectonics and upwelling. GeoArabia 18 (2), 67–94.

Abed, A.M., Al-Agha, M.R., 1989. Petrography, geochemistry and origin of NW Jordan Phosphorites. J. Geol. Soc. London 146, 499–506.

Abu-Ali, R., El-Kammar, A., Zakaria, A., El-Shafeiy, M., Kuss, J., 2019. Paleo-environmental reconstruction of the Late Cretaceous-Paleogene succession, Safaga. Egypt. J. Afr. Earth Sci. 149, 170–193.

Adatte, T., Keller, G., Stinnesbeck, W., 2002. Late Cretaceous to early Paleocene climate and sea-level fluctuations. Palaeog., Palaeoclim. Palaeoec. 2754, 1–32.

Ader, M., Thomazo, C., Sansjofre, P., Busigny, V., Papineau, D., Laffont, R., Cartigny, P., Halverson, G.P., 2016. Interpretation of the nitrogen isotopic composition of Precambrian sedimentary rocks: assumptions and perspectives. Chemical Geol. 429, 93–110.

Algeo, T.J., Lyons, T.W., 2006. Mo-Total organic carbon covariation in modern anoxic marine environments: Implications for analysis of paleoredox and paleohydrographic conditions. Paleoceanography 21 (1). PA1016. https://doi.org/10.1029/2004PA001112, 21.

Algeo, T.J., Rowe, H., 2012. Palaeoceanographic applications of trace-metal concentration data. Chemal Geol. 324–325, 6–18.

Algeo, T.J., Tribovillard, N., 2009. Environmental analysis of paleoceanographic systems based on molybdenum–uranium covariation. Chemical Geol. 268 (3), 211–225.

Almogi-Labin, A., Bein, A., Sass, E., 1993. Late Cretaceous upwelling system along the southern Tethys margins (Israel): interrelationship between productivity, bottom-water environments and organic matter preservation. Paleoceanography 8, 671–690.

Aubry, M-P., 1992. Late Paleogene calcareous nannoplankton evolution: a tale of climatic deterioration. In: Prothero, D.R., Berggren, W.A. (Eds.), Eocene–Oligocene Climatic and Biotic Evolution. Princeton Univ. Press, Princeton, NJ, pp. 272–309.

Awad, M.M., Mohammad, M.H., Atia, G.M., Ramadan, F.S., 1992. Dakhla Shale, Tarawan Chalk and Esna Shale succession, Safaga and Quseir District. Egypt. Proceed. 8th Symp. Phaner. Develop. Egypt, 69–92.

Baioumy, H.M., 2011. Rare earth elements and sulfur and strontium isotopes of upper Cretaceous phosphorites in Egypt. Cretaceous Res. 32, 368–377.

Baioumy, H.M., Eglinton, L.B., Peucker-Ehrenbrink, B., 2011. Re-Os isotopes and PGE systematics of marine vs. non-marine organic-rich sediments from Egypt. Chemical Geol. 285, 70–81.

Baioumy, H.M., Tada, R., 2005. Origin of late Cretaceous phosphorites in Egypt. Cretaceous Res. 26, 261–275.

Barnet, J.S.K., Littler, K., Kroon, D., Leng, M.J., Westerhold, T., Röhl, U., Zachos, J.C., 2018. A new high-resolution chronology for the late Maastrichtian warming event: Establishing robust temporal links with the onset of Deccan volcanism. Geology 46, 147–150.

Barrera, B., Keller, G., 1994. Productivity across the Cretaceous/Tertiary boundary in high latitudes. Geological Soc. Am. Bull. 106, 1254–1266.

Barrier, E., Vrielynck, B., 2008. Paleotectonic maps of the Middle East, Atlas of 14 maps. Tectonosedimentary-Palinspatic maps from Late Norian to Pliocene, Commission for the Geologic Map of the (CCMW-CCGM), Paris, France.

Bartol, M., Pavšič, J., Dobnikar, M., Bernasconi, S.M., 2008. Unusual Braarudosphaera bigelowii and Micrantholithus vesper enrichment in the Early Miocene sediments from the Slovenian Corridor, a seaway linking the Central Paratethys and the Mediterranean. Palaeog., Palaeoclim., Palaeoec., 267 (1–2), 77–88.

Beckmann, B., Flögel, S., Hofmann, P., Schulz, M., Wagner, T., 2005. Orbital forcing of Cretaceous river discharge in tropical Africa and ocean response. Nature 437, 241–244.

Bevan, T.G., Moustafa, A.R., 2012. Inverted Rift-Basins of Northern Egypt. Regional Geology and Tectonics: Phanerozoic Rift Systems and Sedimentary Basins, 1B, 482–507. https://doi.org/10.1016/B978-0-444-56356-9.00018-3.

Birck, J.L., RoyBarman, M., Capmas, F., 1997. Re-Os isotopic measurements at the femtomole level in natural samples. Geostandards Newsl. 21, 19–27.

Bosworth, W., Tari, G., 2021. Hydrocarbon accumulation in basins with multiple phases of extension and inversion: Examples from the Western Desert (Egypt) and the western Black Sea. Solid Ear. 12, 59–77.

Böttcher, M.E., Lepland, A., 2000. Biogeochemistry of sulfur in a sediment core from the west-central Baltic Sea: Evidence from stable isotopes and pyrite textures. J. Marine Sys. 25, 299–312.

Böttcher, M.E., Thamdrup, B., Vennemann, T.W., 2001. Oxygen and sulfur isotope fractionation during anaerobic bacterial disproportionation of elemental sulfur. Geochimica Cosmoch. Act. 65, 1601–1609.

Bown, P.R., Young, J.R., 1998. Techniques. In: Bown, P.R. (Ed.), Calcareous Nannofossil Biostratigraphy. Netherlands Kluwer Academic Publishing, Dordrecht, pp. 16–28.

Bralower, T.J., 2002. Evidence of surface water oligotrophy during the Paleocene-Eocene thermal maximum: Nannofossil assemblage data from ocean drilling program Site 690, Maud rise. Weddell Sea. Paleoceanography 17 (2), 1–13.

Brumsack, H.J., 2006. The trace metal content of recent organic carbon-rich sediments: implications for Cretaceous black shale formation. Palaeog., Palaeoclim. Palaeoec. 232, 344–361.

Canfield, D.E., 1994. Factors influencing organic carbon preservation in marine sediments. Chemical Geol. 114 (3–4), 315–329.

Canfield, D.E., Raiswell, R., Westrich, J.T., Reaves, C.M., Berner, R.A., 1986. The use of chromium reduction in the analysis of reduced inorganic sulfur in sediments and shales. Chem. Geol. 54, 149–155.

Canfield, D.E., Thamdrup, B., Fleischer, S., 1998. Isotope fractionation and sulfur metabolism by pure and enrichment cultures of elemental sulfur-disproportionating bacteria. Limnology Oceanog. 43, 253–264.

Canfield, D.E., Glazer, A.N., Falkowski, P.G., 2010. The evolution and future of Earth's nitrogen cycle. Science 330, 192–196.

Canfield, D.E., Teske, A., 1996. Late Proterozoic rise in atmospheric oxygen concentration inferred from phylogenetic and sulphur-isotope studies. Nature 382, 127–132.

Canfield, D.E., Thamdrup, B., 1994. The production of 34 S-depleted sulfide during bacterial disproportionation of elemental sulfur. Science 266, 1973–1975.

Canfield, D.E., 2001. Biogeochemistry of sulfur isotopes. In: Valley, J.W., Cole, D. (Eds.), Stable Isotope Geochemistry. Mineralogical Society of America and Geochemical Society, Reviews Mineral. and Geochem. 43, 607–636.

Cao, H., He, W., Chen, F., Shan, X., Kong, D., Hou, Q., Pu, X., 2021. Integrated chemostratigraphy (δ13C-δ34S-δ15N) constrains Cretaceous lacustrine anoxic events triggered by marine sulfate input. Chemical Geol. 559, 119912.

Chang, H., Chu, X., Feng, L., Huang, J., Chen, Y., 2018. Marine redox stratification on the earliest Cambrian (ca. 542–529 Ma) Yangtze Platform. Palaeog., Palaeoclim Palaeoec. 504, 75–85.

Chen, G., Chang, X., Gang, W., Wang, N., Zhang, P., Cao, Q., Xu, J., 2020. Anomalous positive pyrite sulfur isotope in lacustrine black shale of the Yanchang Formation, Ordos Basin: Triggered by paleoredox chemistry changes. Marine Pet. Geol., 104587.

Chenet, A.-L., Courtillot, V., Fluteau, F., Gérard, M., Quidelleur, X., Khadri, S.F.R., Subbarao, K.V., Thordarson, T., 2009. Determination of rapid Deccan eruptions across the Cretaceous-Tertiary boundary using paleomagnetic secular variation: 2. Constraints from analysis of eight new sections and synthesis for a 3500-m thick composite section. J. Geophy. Res. 114 (B6), 1–38.

Chu, Z.Y., Yan, Y., Chen, Z., Guo, J.H., Yang, Y.H., Li, C.F., Zhang, Y.B., 2015. A comprehensive method for precise determination of Re, Os, Ir, Ru, Pt, Pd concentrations and Os isotopic compositions in geological samples. Geostandards Geoanal. Res. 39, 151–169.

Cohen, A.S., 2004. The rhenium–osmium isotope system: applications to geochronological and palaeoenvironmental problems. J. Geolog. Soc. Lond. 161, 729–734.

Cohen, A.S., Waters, F.G., 1996. Separation of osmium from geological materials by solvent extraction for analysis by thermal ionisation mass spectrometry. Analytica Chim. Act. 332, 269–275.

Cohen, A.S., Coe, A.L., Harding, S.M., Schwark, L., 2004. Osmium isotope evidence for the regulation of atmospheric CO_2 by continental weathering. Geology 32, 157–160.

Courtillot, V., Besse, J., Vandamme, D., Montigny, R., Jaeger, J.-J., Cappetta, H., 1986. Deccan flood basalts at the Cretaceous/Tertiary boundary? Earth Planet. Sci. Lett. 80, 361–374.

Creaser, R.A., Papanastassiou, D.A., Wasserburg, G.J., 1991. Negative thermal ion mass spectrometry of osmium, rhenium, and iridium. Geochimica Cosmoch. Act. 55, 397–401.

Cullers, R.L., 2002. Implications of elemental concentrations for provenance, redox conditions, and metamorphic studies of shales and limestones near Pueblo, CO, USA. Chemical Geol. 191 (4), 305–327.

Dean, W.E., Arthur, M.A., Claypool, G.E., 1986. Depletion of ^{13}C in Cretaceous marine organic matter: Source, diagenetic, or environmental signal? Marine Geol. 70, 119–157.
Dubin, A., Peucker-Ehrenbrink, B., 2015. The importance of organic-rich shales to the geochemical cycles of rhenium and osmium. Chemical Geol. 403, 111–120.
El-Kammar, M.M., 1993. Organic and inorganic composition of the Upper Cretaceous-Lower Tertiary black shales from Egypt and their hydrocarbon potentialities, Ph.D. Thesis, Faculty of Sciences, Cairo University, 227p.
El-Kammar, A., 2020. Oil Shale of Egypt: The Overlooked Future Energy Resources. In: Zakaria Hamimi, Z., El-Barkooky, A., Frías, J.M., Fritz, H., Abd El-Rahman, Y. (Eds.), The Geology of Egypt, Springer Nature Switzerland AG 2020, doi.org/10.1007/978-3-030-15265-9, pp 659-672.
El-Shafeiy, M., Birgel, D., El-Kammar, A., El-Barkooky, A., Wagreich, M., Mohamed, O., Peckmann, J., 2014. Palaeoecological and post-depositional changes recorded in Campanian-Maastrichtian black shales, Abu Tartur plateau. Egypt. Cretaceous Res. 50, 38–51.
El-Shafeiy, M., Birgel, D., El-Kammar, A., El-Barkooky, A., Wagreich, M., Tahoun, S., Peckmann, J., 2017. Integrated palaeo-environmental proxies of the Campanian to Danian organic-rich Quseir section. Egypt. Marine Pet. Geol. 86, 771–786.
El-Shafeiy, M., 2012. Characterization and Economic Potentiality of Oil shales in Al-Quseir and Abu Tartur areas, Egypt. Unpublished PhD thesis, Cairo Uni., 145 pp.
El-Shafeiy, El-Kammar, A., El-Barkooky, A., Meyers, P., 2016. Paleo-redox depositional conditions inferred from trace metal accumulation in two Cretaceous-Paleocene organic-rich sequences from Central Egypt. Marine Pet. Geol. 73, 333-349.
Eshet, Y., Almogi-Labin, A., Bein, A., 1994. Dinofagellate cysts, paleoproductivity and upwelling systems: a Late Cretaceous example from Israel. Marine Micropal. 18, 199–228.
Erba, E., 1992. Middle Cretaceous calcareous nannofossils from the western Pacific (ODP Leg 129), evidence for palaeoequatorial crossings. Proceedings of the ODP, Sci. Results 129, 189–201.
Eshet, Y., Almogi-Labin, A., 1996. Calcareous nannofossils as paleoproductivity indicators in Upper Cretaceous organic-rich sequences in Israel. Marine Micropal. 29 (1), 37–61.
Eshet, Y., Moshkovitz, S., Habib, D., Benjamini, C., Magaritz, M., 1992. Calcareous nannofossil and dinoƐagellate stratigraphy across the Cretaceous/Tertiary boundary at Hor Hahar. Israel. Marine Micropal. 18, 199–228.
Esmeray-Senlet, S., Wright, J.D., Olsson, R.K., Miller, K.G., Browning, J.V., Quan, T.M., 2015. Evidence for reduced export productivity following the Cretaceous/Paleogene mass extinction. Paleoceanography 30, 718–738. https://doi.org/10.1002/2014PA002724.
Falkowski, P.G., Katz, M.E., Knoll, A.H., Quigg, A., Raven, J.A., Schofield, O., Taylor, F.J. R., 2004. The Evolution of Modern Eukaryotic Phytoplankton. Science 305, 354–360.
Fathy, D., Wagreich, M., Zaki, R., Mohamed, R.S.A., Gier, S., 2018. Geochemical fingerprinting of Maastrichtian oil shales from the Central Eastern Desert, Egypt: implications for provenance, tectonic setting, and source area weathering. Geological J. 53, 2597–2612.
Fathy, D., Wagreich, M., Fathi, E., Ahmed, M.S., Leila, M., Sami, M., 2023a. Maastrichtian anoxia and its influence on organic matter and trace metal patterns in the Southern Tethys realm of Egypt during greenhouse variability. ACS Omega 8, 19603–19612. https://doi.org/10.1021/acsomega.3c01096.
Faris, M., Shabaan, M., Shaker, F., 2017. Calcareous nannofossil bioevents at the Paleocene/Eocene boundary in Kharga Oasis, Western Desert of Egypt. Geol. Croat. 70 (3), 179–199.
Fathy, D., Abart, R., Wagreich, M., Gier, S., Ahmed, M.S., Sami, M., 2023b. Late Campanian Climatic-Continental Weathering Assessment and Its Influence on Source Rocks Deposition in Southern Tethys. Egypt. Minerals 13, 160. https://doi.org/10.3390/min13020160.
Fedo, C.M., Nesbitt, H.W., Young, G.M., 1995. Unraveling the effects of potassium metasomatism in sedimentary rocks and paleosols, with implications for paleoweathering conditions and provenance. Geology 23 (10), 921–924.
Firth, J.V., Wise Jr., S.W., 1992. A preliminary study of the evolution of Chiasmolithus in the middle Eocene to Oligocene of Sites 647 and 748, ODP Leg 120. Proceedings of the Ocean Drilling Program, Scientific Results 120, 493–508.
Freeman, K.H., 2001. Isotopic Biogeochemistry of Marine Organic Carbon. In: Valley, J.W., Cole, D. (Eds.), Stable Isotope Geochemistry. Mineralogical Society of America and Geochemical Society, Reviews Mineral. Geochem. 43, 579–606.
Fry, B., Jannasch, H.W., Molyneaux, S.J., Wirsen, C.O., Muramoto, J. A., King, S., 1991. Stable isotope studies of the carbon, nitrogen and sulfur cycles in the Black Sea and the Cariaco Trench. Deep-Sea Res. 38 (Suppl. 2), S1003-S1019.
Fry, B., Ruf, W., Gest, H., Hayes, J.M., 1988. Sulfur isotope effects associated with oxidation of sulfide by O_2, in aqueous solution. Chemical Geol. 73, 205–210.
Ganz, H., 1984. Organic geochemical and palynological studies of a Dakhla Shale profile in Southeast Egypt. Part B. Origin of the organic matter and its relation to phosphorites formation. Berliner Geowiss. Abhand. (a) 50, 363–374.
Garver, J.I., Royce, P.R., Smick, T.A., 1996. Chromium and nickel in shale of the Taconic Foreland: a case study for the provenance of fine-grained sediments with an ultramafic source. J. Sediment. Res. 100 (1), 100–106.
Garecka, M., 2012. Record of changes in the Oligocene-Miocene sediments of the Menilite-Krosno series of the Skole unit based on calcareous nannoplankton studies-biostratigraphy and palaeogeographical implications (Polish Outer Carpathians). Biul. - Panstw. Inst. Geol. 453 (453), 1–22.
Germann, K., Bock, W.D., Schröter, T., 1985. Properties and origin of Upper Cretaceous Campanian phosphorites in Egypt. Sciences Géol. Bull. Mém. 77, 23–33.
Gibbs, S.J., Bown, P.R., Sessa, J.A., Bralower, T.J., Wilson, P.A., 2006. Nannoplankton extinction and origination across the Paleocene-Eocene Thermal Maximum. Science 314 (5806), 1770–1773.
Glenn, C., Arthur, A., 1990. Anatomy and origin of a Cretaceous phosphorite-greensand giant. Egypt. Sedimentology 37, 132–154.
Gradstein, F., Ogg, J., Smith, A., 2004. A Geologic Time Scale. Cambridge University Press, Cambridge, UK, p. 598.
Guiraud, R., Bosworth, W., 1999. Phanerozoic geodynamic evolution of northeastern Africa and the northwestern Arabian platform. Tectonophysics 315, 73–108.
Guiraud, R., Bosworth, W., Thierry, J., Delplanque, A., 2005. Phanerozoic geological evolution of Northern and Central Africa: An overview. J. Afr. Earth Sci. 43, 83–143.
Hallock, P., 1987. Fluctuations in the trophic resource continuum: a factor in global diversity cycles? Paleoceanography 2 (5), 457–471.
Hammer, Ø., Harper, D.A.T., Ryan, P.D., 2001. PAST: Paleontological Statistics Software Package for Education and Data Analysis. Palaeontologia Electron. 4, 1–9.
Hammer, Ø., Harper, D.A.T., 2006. Paleontological Data Analysis. Blackwell 351.
Hayashi, K.I., Fujisawa, H., Holland, H.D., Ohmoto, H., 1997. Geochemistry of ~1.9 Ga sedimentary rocks from northeastern Labrador. Canada. Geochimica Cosmoch. Act. 61 (19), 4115–4137.
Hayes, J.M., Strauss, H., Kaufman, A.J., 1999. The abundance of 13C in marine organic matter and isotopic fractionation in the global biogeochemical cycle of carbon during the past 800 Ma. Chemical Geol. 161, 103–125.
Helz, G.R., Bura-Nakić, E., Mikac, N., Ciglenečki, I., 2011. New model for molybdenum behavior in euxinic waters. Chemical Geol. 284, 323–332.
Henehan, M.J., Hull, P.M., Penman, D.E., Rae, J.W.B., Schmidt, D.N., 2016. Biogeochemical significance of pelagic ecosystem function: An end-Cretaceous case study. Phil. Trans. R. Soc. B371: 20150510.http://dx.doi.org/10.1098/rstb.2015.0510.
Hiscott, R.N., 1984. Clay mineralogy and clay-mineral provenance of Cretaceous and Paleogene strata, Labrador and Baffin shelves. Bulletin Canad. Pet. Geol. 32 (3), 272–280.
Höntzsch, S., Scheibner, C., Guasti, E., Kuss, J., Marzouk, A.M., Rasser, M.W., 2011. Increasing restriction of the Egyptian shelf during the Early Eocene? — New insights from a southern Tethyan carbonate platform. Palaeog., Palaeoclim. Palaeoec. 302, 349–366.
Huber, B.T., MacLeod, K.G., Tur, N.A., 2008. Chronostratigraphic framework for upper Campanian-Maastrichtian sediments on the Blake Nose (subtropical North Atlantic). J. Foraminiferal Res. 38 (2), 162–182.
Huber, B.T., Watkins, D.K., 1992. Biogeography of Campanian– Maastrichtian calcareous plankton in the region of the Southern Ocean: paleogeographic and paleoclimatic implications. In: The Antarctic paleoenvironment: a perspective on global change. Antarctic Research Series 56, 31–60.
Hull, P.M., Bornemann, A., Penman, D., Henehan, M.J., Norris, R.D., Wilson, P.A., Blum, P., Alegret, L., Batenburg, S., Bown, P.R., Bralower, T.J., Cournede, C., Deutsch, A., Donner, B., Friedrich, O., Jehle, S., Kim, H., Kroon, D., Lippert, P., Loroch, D., Moebius, I., Moriya, K., Peppe, D.J., Ravizza, D.E., Röhl, U., Schueth, J. D., Sepúlveda, J., Sexton, P., Sibert, E., Śliwińska, K.K., Summons, R.E., Thomas, E., Westerhold, T., Whiteside, T.J., Yamaguchi, T., Zachos, J.C., 2020. On impact and volcanism across the Cretaceous-Paleogene boundary. Science 367, 266–272.
Issawi, B., Farouk, S., 2023. An Overview of the Phanerozoic Geology in Egypt. In: Hamimi, Z., Khozyem, H., Adatte, T., Nader, F.H., Oboh-Ikuenobe, F., Zobaa, M.K., El Atfy, H. (Eds.), The Phanerozoic Geology and Natural Resources of Egypt. Springer Nature Switzerland AG, 3-26pp.
Keller, G., 2003. Biotic effects of impacts and volcanism. Earth Planet. Sci. Lett. 215, 249–264.
Keller, G., Adatte, T., Stinnesbeck, W., Stuben, D., Kramar, U., Berner, Z., Li, L., Perch-Nielsen, K., 1998. The Cretaceous-Tertiary transition in the shallow Saharan platform of southern Tunisia. Geobios 30, 951–975.
Keller, G., Adatte, T., Burns, S.J., Tantawy, A.A., 2002. High-stress paleoenvironment during the late Maastrichtian to early Paleocene in central Egypt. Palaeog., Palaeoclim. Palaeoec. 187, 35–60.
Keller, G., Bhowmick, P.K., Upadhyay, H., Dave, A., Reddy, A.N., Jaiprakash, B.C., Adatte, T., 2011. Deccan Volcanism Linked to the Cretaceous-Tertiary Boundary Mass Extinction: New Evidence from ONGC Wells in the Krishna-Godavari Basin. J. Geol. Soc. India 78, 399–428.
Keller, G., Adatte, T., Bhowmick, P.K., Upadhyay, H., Dave, A., Reddy, A.N., Jaiprakash, B.C., 2012. Nature and timing of extinctions in Cretaceous-Tertiary planktic foraminifera preserved in Deccan inter trappean sediments of the Krishnae Godavari Basin. India. Earth Planet. Sci. Lett. 341, 211–221.
Keller, G., Punekar, J., Mateo, P., 2016. Upheavals during the Late Maastrichtian: Volcanism, climate and faunal events preceding the end-Cretaceous mass extinction. Palaeog., Palaeoclim Palaeoec. 441, 137–151.
Khalil, S.M., McClay, K.R., 2002. Extensional fault-related folding, northwestern Red Sea, Egypt. J. Struct. Geol. 24, 743–762.
Khalil, S.M., McClay, K.R., 2009. Structural control on syn-rift sedimentation, northwestern Red Sea margin. Egypt. Marine Pet. Geol. 26, 1018–1034.
Kodina, L.A., 2002. Carbon isotope composition of phytoplankton in the Yenisei river estuary-open sea system and the application of isotopic approach for evaluation

of phytoplankton contribution to the Yenisei POC load. Reports Polar Mar. Res. 419, 143–150.
Küspert, W., 1982. Environmental changes during oil shale deposition as deduced from stable isotope ratios. In: Einsele, G., Seilacher, A. (Eds.), Cyclic and Event Stratification: Heidelberg. Springer, pp. 482–501.
Kuypers, M.M.M., van Breugel, Y., Schouten, S., Erba, E., Sinninghe Damsté, J.S., 2004. N_2-fixing cyanobacteria supplied nutrient N for Cretaceous oceanic anoxic events. Geology 32, 853–856.
Legendre, P., Legendre, L., 1998. Numerical Ecology, Volume 24, 2nd Edition, Elsevier.
Lees, J.A., 2002. Calcareous nannofossil biogeography illustrates palaeoclimate change in the Late Cretaceous Indian Ocean. Cretaceous Res. 23 (5), 537–634.
Lehman, M.F., Bernasconi, S.M., Barbieri, A., McKenzie, J.A., 2002. Preservation of organic matter and alteration of its carbon and nitrogen isotope composition during simulated and in situ early sedimentary diagenesis. Geochimica Cosmoch. Act. 66, 3573–3584.
Li, L., Keller, G., 1998. Abrupt deep-sea warming at the end of the Cretaceous. Geology 26, 995–999.
Li, L., Keller, G., Stinnesbeck, W., 1999. The Late Campanian and Maastrichtian in northwestern Tunisia: paleoenvironmental inferences from lithology, macrofauna and benthic foraminifera. Cretaceous Res. 20, 231–252.
Libes, S.M., Deuser, W.G., 1988. The isotope geochemistry of particulate nitrogen in the Peru upwelling area and the gulf of Maine. Deep Sea Res. Part a: Oceanogr. Res. Pap. 35, 517–533.
Linnert, C., Robinson, S.A., Lees, J.A., Bown, P.R., Pérez-Rodríguez, I., Petrizzo, M.R., Falzoni, F., Littler, K., Arz, J.A., Russell, E.E., 2014. Evidence for global cooling in the Late Cretaceous. Nature Comm. 5 (1), 1–7.
Linnert, C., Robinson, S., Lees, J., Pérez-Rodríguez, I., Jenkyns, H., Petrizzo, M., Arz, J., Bown, P., Falzoni, F., 2017. Did Late Cretaceous cooling trigger the Campanian-Maastrichtian boundary event? Newsletters on Stratig. 50 (2), 1–16.
Littke, R., Zieger, L., 2020. Formation of Organic-Rich Sediments and Sedimentary Rocks. In: Wilkes, H. (Ed.), Hydrocarbons, Oils and Lipids: Diversity, Origin, Chemistry and Fate, Handbook of Hydrocarbon and Lipid Microbiology, Springer Nature Switzerland, doi.org/10.1007/978-3-319-90569-3_14, pp. 475-492.
Luger, P., 1988. Maastrichtian to Paleocene facies evolution and Cretaceous/Tertiary boundary in middle and southern Egypt. Rev. Espan. Micropaleont. No. Extraordinario, 83–90.
McArthur, J.M., Algeo, T.J., van de Schootbrugge, B., Li, Q., Howarth, R.J., 2008. Basinal restriction, black shales, Re–Os dating, and the Early Toarcian (Jurassic) oceanic anoxic event. Paleoceanography 23, 1607–1614. https://doi.org/10.1029/2008PA001607.
McKay, J.L., Longstaffe, F.J., 2003. Sulfur isotope geochemistry of pyrite from the Upper Cretaceous Marshybank formation, Western Interior Basin. Sedimentary Geol. 157, 175–195.
McLennan, S.M., 1993. Weathering and global denudation. J. Geol. 101 (2), 295–303.
McLennan, S.M., Taylor, S.R., 1991. Sedimentary rocks and crustal evolution: tectonic setting and secular trends. J. Geol. 99 (1), 1–21.
McLennan, S.M., Hemming, S., McDaniel, D.K., Hanson, G.N., 1993. Geochemical approaches to sedimentation, provenance, and tectonics. In: Johnson, M.J., Basu, A. (Eds.), Processes Controlling the Composition of Clastic Sediments. Geological Society of America, Boulder, CO, pp. 21–40.
Meilijson, A., Ashckenazi-Polivoda, S., Illner, P., Speijer, R.P., Almogi-Labin, A., Feinstein, S., Püttmann, W., Abramovich, S., 2018. From phytoplankton to oil shale reservoirs: A 19-million-year record of the Late Cretaceous Tethyan upwelling regime in the Levant Basin. Marine Pet. Geol. 95, 188–205.
Meyers, P.A., 1992. Changes in organic carbon stable isotope ratios across the K/T boundary: global or local control? Chemical Geol. 101, 283–291.
Meyers, P.A., 1994. Preservation of elemental and isotopic source identification of sedimentary organic matter. Chemical Geol. 114, 289–302.
Meyers, P.A., 1997. Organic geochemical proxies of paleoceanographic, paleolimnologic, and paleoclimatic processes. Org. Geochem. 27 (5/6), 213–250.
Meyers, P.A., Yuma, J.G., Wise, S.W., 2009. Origins and maturity of organic matter in mid-Cretaceous black shales from ODP Site 1138 on the Kerguelen Plateau. Marine Pet. Geol. 26, 909–915.
Miller, A.J., Strauss, J.V., Halverson, G.P., Macdonald, F.A., Johnston, D.T., Sperling, E. A., 2017. Tracking the onset of Phanerozoic-style redox-sensitive trace metal enrichments: new results from basal Ediacaran post-glacial strata in NW Canada. Chemical Geol. 457, 24–37. https://doi.org/10.1016/j.chemgeo.2017.03.010.
Milligan, J.N., Royer, D.L., Franks, P.J., Upchurch, G.R., McKee, M.L., 2019. No Evidence for a Large Atmospheric CO2 Spike Across the Cretaceous-Paleogene Boundary. Geophys. Res. Lett. 46, 3462–3472. https://doi.org/10.1029/2018GL081215.
Monechi, S., Buccianti, A., Gardin, S., 2000. Biotic signals from nannoflora across the iridium anomaly in the upper Eocene of the Massignano section: evidence from statistical analysis. Marine Micropal 39 (1–4), 219–237.
Nesbitt, H.W., Young, G.M., 1982. Early Proterozoic climates and plate motions inferred from major element chemistry of lutites. Nature 299, 715–717.
Nordt, L., Atchley, S., Dworkin, S., 2003. Terrestrial evidence for two greenhouse events in the latest Cretaceous. GSA Today 13 (12), 4–9.
Panahi, A., Young, G.M., Rainbird, R.H., 2000. Behavior of major and trace elements (including REE) during Paleoproterozoic pedogenesis and diagenetic alteration of an Archean granite near Ville Marie, Quebec. Canada. Geochimica Cosmoch. Act. 64 (13), 2199–2220.
Pasquier, V., Fike, D.A., Halevy, I., 2021. Sedimentary pyrite sulfur isotopes track the local dynamics of the peruvian oxygen minimum zone. Nature Comm. 12, 4403.
Perch-Nielsen, K., 1979. Calcareous nannofossils from the Cretaceous between the North Sea and the Mediterranean. In: Aspekte der Kreide Europas. IUGS Series A 6, 223–272.
Perch-Nielsen, K., 1985. Mesozoic calcareous nannofossils. In: Bolli, H.M., Saunders, J.B., Perch-Nielsen, K. (Eds.), Plankton stratigraphy. Cambridge University Press, pp. 329–426.
Persico, D., Villa, G., 2004. Eocene–Oligocene calcareous nannofossils from Maud Rise and Kerguelen Plateau (Antarctica): paleoecological and paleoceanographic implications. Marine Micropal 52 (1–4), 153–179.
Peterson, B.J., Howarth, R.W., 1987. Sulfur, carbon, and nitrogen isotopes used to trace organic matter flow in the salt-marsh estuaries of Sapelo Island, Georgia. Limnol. Oceanog. 32, 1195–1213.
Peucker-Ehrenbrin, B., Ravizza, G., 1996. Continental runoff of osmium into the Baltic Sea. Geology 24 (4), 327–330.
Peucker-Ehrenbrink, B., Blum, J.D., 1998. Re-Os isotope systematics and weathering of Precambrian crustal rocks: implications for the marine Os isotope record. Geochimica Cosmoch. Act. 62, 3193–3203.
Peucker-Ehrenbrink, B., Jahn, B.M., 2001. Rhenium–osmium isotope systematics and platinum group element concentrations: loess and the upper continental crust. Geochem. Geophys. Geosyst. 2 (10), 2200. https://doi.org/10.1029/2001GC000172.
Peucker-Ehrenbrink, B., Ravizza, G., 2000. The marine osmium isotope record. Terra Nova 12, 205–219.
Peucker-Ehrenbrink, B., Ravizza, G., 2002. The marine osmium isotope record. Terra Nov. 12, 205–219.
Phillips, R., Xu, J., 2021. A critical review of molybdenum sequestration mechanisms under euxinic conditions: Implications for the precision of molybdenum paleoredox proxies. Earth-Sci. Rev. 221, 103799.
Pinti, D.L., Hashizume, K., 2011. Early life record from nitrogen isotopes. In: Golding, S.D., Glikson, M. (Eds.), Earliest Life on Earth: Habitats, Environments and Methods of Detection. Springer, Berlin, pp. 183–205.
Pospichal, J.J., 1996. High latitude calcareous nannofossil changes at the Cretaceous/Tertiary boundary in the southern Indian Ocean. In: Microfossils and Oceanic Environments. University of Wales, Aberystwyth-Press, pp. 205–229.
Pospichal, J.J., Wise Jr., S.W., 1990. Maestrichtian calcareous nannofossil biostratigraphy of Maud rise ODP Leg 113 Sites 689 and 690, Weddell Sea. Proc. ODP, Sci. Results 113, 465–487.
Prahl, F.G., Cowie, G.L., De Lange, G.J., Sparrow, M.A., 2003. Selective organic matter preservation in "burn-down" turbidites on the Madeira Abyssal Plain. Paleoceanography 18 (2), 1052. https://doi.org/10.1029/2002PA000853.
Punekar, J., Keller, G., Khozyem, H., Hamming, C., Adatte, T., Tantawy, A.A., Spangenberg, J.E., 2014. Late Maastrichtian–early Danian high-stress environments and delayed recovery linked to Deccan volcanism. Cretaceous Res. 49, 63–82.
Ravizza, G., 2001. Platinum group elements and their isotopes. In: Steele, J.H., Turekian, K.K., Thorpe, S.A. (Eds.), Encyclopedia of Ocean Sciences 4 (n-r). Academic Press, Dordrecht, pp. 2208–2217. https://doi.org/10.1006/rwos.2001.0286.
Ravizza, G., Esser, B.K., 1993. A possible link between the sea water osmium isotope record and weathering of ancient sedimentary organic matter. Chem. Geol. 107, 255–258.
Ravizza, G., VonderHaar, D., 2012. A geochemical clock in earliest Paleogene pelagic carbonates based on the impact-induced Os isotope excursion at the Cretaceous-Paleogene boundary. Paleoceanography 27, PA3219. https://doi.org/10.1029/2012PA002301.
Ravizza, G., Norris, R.N., Blusztajn, J., Aubry, M.P., 2001. An osmium isotope excursion associated with the late Paleocene thermal maximum: Evidence of intensified chemical weathering. Paleoceanography 16, 155–163.
Ravizza, G., Peucker-Ehrenbrink, B., 2003. Chemostratigraphic evidence of Deccan volcanism from the marine osmium isotope record. Science 302 (5649), 1392–1395.
Rieu, R., Allen, P.A., Plötze, M., Pettke, T., 2007. Climatic cycles during a Neoproterozoic "snowball" glacial epoch. Geology 35 (4), 299–302.
Robinson, V.D., 1995. Source rock characterization of the late cretaceous brown limestone of Egypt. In: Katz, B. (Ed.), Petroleum Source Rocks. Springer, Berlin, pp. 265–281.
Robinson, V., Engel, M., 1993. Characterization of the source horizons within the Late Cretaceous transgressive sequence of Egypt. In: Katz, B., Pratt, L. (Eds.), Source Rocks in a Sequence Stratigraphic Framework, Studies in Geology-. American Association of Petroleum Geologists (101–117).
Robinson, R.S., Kienast, M., Albuquerque, A.L., Altabet, M., Contreras, S., Holz, R.D.P., Dubois, N., Francois, R., Galbraith, E., Hsu, T.C., Ivanochko, T., Jaccard, S., Kao, S.J., Kiefer, T., Kienast, S., Lehmann, M.F., Martinez, P., McCarthy, M., Mobius, J., Pederson, T., Quan, T.M., Ryabenko, E., Schmittner, A., Schneider, R., Schneider-Mor, A., Shigemitsu, M., Sinclair, D., Somes, C., Studer, A., Thunell, R., Yang, J.Y., 2012. A review of nitrogen isotopic alteration in marine sediments. Paleoceanography 27, PA4203.
Robinson, N., Ravizza, G., Coccioni, R., Peucker-Ehrenbrink, B., Norris, R., 2009. A high-resolution marine 187Os/188Os record for the late Maastrichtian: Distinguishing the chemical fingerprints of Deccan volcanism and the KP impact event. Earth Planet. Sci. Lett. 281 (3–4), 159–168.
Rosenberg, Y.O., Ashckenazi-Polivoda, S., Abramovich, S., Thibault, N., Chin, S., Feinstein, S., Bartov, Y., Amrani, A., 2021. Resilience of primary and export

productivity in a eutrophic ecosystem following the Cretaceous-Paleogene mass extinction. Global Planet. Chang. 196, 103371.
Roth, P.H., 1978. Cretaceous nannoplankton biostratigraphy and oceanography of the northwestern Atlantic Ocean. Initial Reports of the DSDP 44, 731–760.
Roth, P.H., Bowdler, J.L., 1981. Middle Cretaceous calcareous nannoplankton biogeography and oceanography of the Atlantic Ocean. SEPM, Spec. Publ. 32, 517–546.
Roth, P.H., Krumbach, K.R., 1986. Middle Cretaceous calcareous nannofossil biogeography and preservation in the Atlantic and Indian oceans: implications for palaeoceanography. Marine Micropal. 10, 235–266.
Roy, D.K., Roser, B.P., 2013. Climatic control on the composition of Carboniferous-Permian Gondwana sediments, Khalaspir basin. Bangladesh. Gondwana Res. 23 (3), 1163–1171.
Said, R., 1990. Cretaceous paleogeographic maps. In: Said, R. (Ed.), The Geology of Egypt. A.A, Balkema, Rotterdam, pp. 439–449.
Schneider-Mor, A., Alsenz, H., Ashckenazi-Polivoda, S., Illner, P., Abramovich, S., Feinstein, S., Almogi-Labin, A., Berner, Z., Püttmann, W., 2012. Paleoceanographic reconstruction of the late Cretaceous oil shale of the Negev, Israel: integration of geochemical and stable isotope records of the organic matter. Palaeog., Palaeoclim Palaeoec. 319–320, 46–57.
Schouten, S., Van Kaam-Peters, H.M.E., Rijpstra, W.I.C., Schoell, M., Sinninghe Damste, J.S., 2000. Effects of an oceanic anoxic event on the stable carbon isotopic composition of early Toarcian carbon. American J. Sci. 300, 1–22.
Scott, C., Lyons, T.W., Bekker, A., Shen, Y., Poulton, S.W., Chu, X., Anbar, A.D., 2008. Tracing the stepwise oxygenation of the Proterozoic ocean. Nature 452, 456–459.
Scott, C., Lyons, T.W., 2012. Contrasting molybdenum cycling and isotopic properties in euxinic versus non-euxinic sediments and sedimentary rocks: Refining the paleoproxies. Chemical Geol. 324, 19–27.
Selby, D., Creaser, R.A., 2003. Re–Os geochronology of organic rich sediments: an evaluation of organic matter analysis methods. Chemical Geol. 200, 225–240.
Sepúlveda, J., Alegret, L., Thomas, E., Haddad, E., Cao, C., Summons, R. E., 2019. Stable isotope constraints on marine productivity across the Cretaceous-Paleogene mass extinction. Paleoceanography Paleoclim. 34, 1195–1217. doi.org/10.1029/2018PA003442.
Sepúlveda, J., Wendler, J.D., Summons, R.E., Hinrichs, K.-W., 2009. Rapid Resurgence of Marine Productivity after the Cretaceous-Paleogene Mass Extinction Event. Nature 326, 129–132.
Sepúlveda, J., 2008. Ecological and environmental consequences of Oceanic Anoxic Events and the Cretaceous-Paleogene mass extinction event: a molecular-isotopic approach, PhD thesis, Bremen University, Germany. https://media.suub.uni-bremen.de/bitstream/elib/2576/1/00011217.pdf.
Sharp, Z., 2017. Principles of Stable Isotope Geochemistry, 2nd Edition. doi: https://doi.org/10.25844/h9q1-0p82.
Shafik, S., 1990. Late Cretaceous nannofossil biostratigraphy and biogeography of the Australian western margin. Bur. Miner. Resour. Geol. Geophys. Rep. (Canberra) 295, 1–164.
Shirey, S.B., Walker, R.J., 1995. Carius tube digestion for low-blank rhenium-osmium analysis. Analytical Chem. 67, 2136–2141.
Shirey, S.B., Walker, R.J., 1998. The Re-Os isotope system in cosmochemistry and high-temperature geochemistry. Annual Rev. Earth Planet. Sci. Lett. 26, 423–500.
Sial, A.N., Chen, J., Lacerda, L.D., Frei, R., Tewari, V.C., Pandit, M.K., Gaucher, C., Ferreira, V.P., Cirilli, S., Peralta, S., Korte, C., Barbosa, J.A., Pereira, N.S., 2016. Mercury enrichment and Hg isotopes in Cretaceous-Paleogene boundary successions: Links to volcanism and palaeoenvironmental impacts. Cretaceous Res. 66, 60–81.
Sim, M.S., Bosak, T., Ono, S., 2011. Large sulfur isotope fractionation does not require disproportionation. Science 333, 74–77.
Soliman, M.F., El Goresy, A., 2012. Framboidal and idiomorphic pyrite in the upper Maastrichtian sedimentary rocks at Gabal Oweina, Nile Valley, Egypt: Formation processes, oxidation products and genetic implications to the origin of framboidal pyrite. Geochimica Cosmoch. Act. 90, 195–220.
Sun, W., Bennett, V.C., Eggins, S.M., Kamenetsky, V.S., Arculus, R.J., 2003. Enhanced mantle-to-crust rhenium transfer in undegassed arc magmas. Nature 422, 294–297.
Tahoun, S.S., Mohamed, O., 2020. Distribution of peridiniacean dinoflagellate cysts from cores of organic rich shales of the Duwi and Dakhla formations of Egypt. J. Afr. Earth Sci. 170, 103892.
Takashima, R., Nishi, H., Huber, B., Leckie, R.M., 2006. Greenhouse world and the Mesozoic ocean. Oceanography 19 (4), 82–92.
Tantawy, A.A., 2003. Calcareous nannofossil biostratigraphy and paleoecology of the Cretaceous-Tertiary transition in the central eastern desert of Egypt. Marine Micropal. 47 (3–4), 323–356.
Taylor, S.R., McLennan, S.M., 1985. The Continental Crust: Its Composition and Evolution. Blackwell, London, p. 312.
Thibault, N., Husson, D., 2016. Climatic fluctuations and sea-surface water circulation patterns at the end of the Cretaceous era: Calcareous nannofossil evidence. Palaeog., Palaeoclim Palaeoec. 441, 152–164.
Thibault, N., Gardin, S., 2006. Maastrichtian calcareous nannofossil biostratigraphy and paleoecology in the Equatorial Atlantic (Demerara Rise, ODP Leg 207 Hole 1258A). Rev. Micropaléontol. 49 (4), 199–214.
Thibault, N., Harlou, R., Schovsbo, N.H., Stemmerik, L., Surlyk, F., 2016. Late Cretaceous (late Campanian–Maastrichtian) sea-surface temperature record of the Boreal Chalk Sea. Climate past 12 (2), 429–438.
Thierstein, H.R., 1976. Mesozoic calcareous nannoplankton biostratigraphy of marine sediments. Marine Micropal 1, 325–362.
Thierstein, H.R., 1981. Late Cretaceous nannoplankton and the change at the Cretaceous-Tertiary boundary. SEPM Spec. Publ. 32, 355–394.
Thunell, R.C., Sautter, L.R., 1992. Planktonic foraminiferal, fauna and stable isotope indices of upwelling: a sediment trap study in the San Pedro Basin, Southern California Bight. In: Summerhayes, C.P., Prell, W.L., Emeis, K.C. (Eds.), Upwelling system: evolution since the Early Miocene. Geological Soc. Spec. Publ. 64, 77-91.
Tribovillard, N., Algeo, T.J., Lyons, T., Riboulleau, A., 2006. Trace metals as palaeoredox and palaeoproductivity proxies: an update. Chemical Geol. 232, 12–32.
Van Simaeys, S., De Man, E., Vandenberghe, N., Brinkhuis, H., Steurbaut, E., 2004. Stratigraphic and palaeoenvironmental analysis of the Rupelian–Chattian transition in the type region: evidence from dinoflagellate cysts, foraminifera and calcareous nannofossils. Palaeog., Palaeoclim., Palaeoec. 208 (1–2), 31–58.
Wade, B.S., Pearson, P.N., Berggren, W.A., Pälike, H., 2011. Review and revision of Cenozoic tropical planktonic foraminiferal biostratigraphy and calibration to the geomagnetic polarity and astronomical time scale. Earth-Sci. Rev. 104 (1–3), 111–142.
Watkins, D.K., 1992. Upper Cretaceous nannofossils from Leg 120, Kerguelen Plateau, Southern Ocean. Proc. ODP, Sci. Results 120, 343–370.
Watkins, D.K., Wise, S.W., Pospichal, J.J., Crux, J., 1996. Upper Cretaceous calcareous nannofossil biostratigraphy and paleoceanography of the Southern Ocean. In: Moguilevsky, A., Whatley, R. (Eds.), Microfossils and oceanic environments. University of Wales, Aberystwyth Press, pp. 355–381.
Wei, W., Villa, G., Wise, S.W., 992. Paleoceanographic Implications of Eocene-Oligocene Calcareous nannofossils from sites 711 and 748 in the Indian Ocean. Proc. ODP, Sci. Results 120, 979–999.
Wei, W., Wise Jr., S.W., 1990. Biogeographic gradients of middle Eocene-Oligocene calcareous nannoplankton in the South Atlantic Ocean. Palaeog., Palaeoclim Palaeoec. 79 (1–2), 29–61.
Williams, J.R., Bralower, T.J., 1995. Nannofossil assemblages, fine fraction stable isotopes, and the paleoceanography of the Valanginian-Barremian (Early Cretaceous) North Sea Basin. Paleoceanography 10 (4), 815–839.
Yamashita, Y., Takahashi, Y., Haba, H., Enomoto, S., Shimizu, H., 2007. Comparison of reductive accumulation of Re and Os in seawater–sediment systems. Geochimica Cosmoch. Act. 71, 3458–3475.
Yarincik, K.M., Murray, R.W., Peterson, L.C., 2000. Climatically sensitive eolian and hemipelagic deposition in the Cariaco Basin, Venezuela, over the past 578,000 years: results from Al/Ti and K/Al. Paleoceanography 15 (2), 210–228.
Yin, L., Zhao, P., Liu, J., Li, J., 2023. Re-Os isotope system in organic-rich samples for dating and tracing: Methodology, principle, and application. Earth-Sci. Rev. 238, 104317.
Young, J.R., 1994. Functions of coccoliths. In: Winter, A., Siesser, W.G. (Eds.), Coccolithophores. Cambridge University Press, Cambridge, pp. 63–82.
Zalat, A.A., Ramadan, F.S., El Safori, Y.A., 2008. Campanian-Paleocene facies, depositional environments and paleoclimitic conditions along the Red Sea coast, Egypt. 3rd Env. Conf. Faculty of Sci. Zagazig Uni, pp. 187–225.
Zhai, L.N., Wu, C.D., Ye, Y.T., Zhang, S.C., Wang, Y.Z., 2018. Fluctuations in chemical weathering on the Yangtze Block during the Ediacaran-Cambrian transition: Implications for paleoclimatic conditions and the marine carbon cycle. Palaeog., Palaeoclim Palaeoec. 490, 280–292.
Zhang, G., Chen, D., Huang, K.-J., Liu, M.u., Huang, T., Yeasmin, R., Fu, Y., 2021. Dramatic attenuation of continental weathering during the Ediacaran-Cambrian transition: Implications for the climatic-oceanic-biological co-evolution. Global Planet. Chang. 203, 103518.
Zhang, S.C., Wang, X.M., Hammarlund, E.U., Wang, H.J., Costa, M.M., Bjerrum, C.J., Connelly, J.N., Zhang, B.M., Bian, L.Z., Canfield, D.E., 2015. Orbital forcing of climate 1.4 billion years ago. Proceeding Nat. Acad. Sci. USA 112 (12), E1406–E1413.